fluids

MDPI

Article

Compressing Magnetic Fields by the Electromagnetic Implosion of a Hollow Lithium Cylinder: Experimental Test Beds Simulated with OpenFOAM

Victoria Suponitsky *,†, Ivan V. Khalzov †, David M. Roberts † and Piotr W. Forysinski †

General Fusion, 6020 Russ Baker Way, Richmond, BC V7B 1B4, Canada; ivan.khalzov@generalfusion.com (I.V.K.); david-roberts-@hotmail.com (D.M.R.); piotr.forysinski@generalfusion.com (P.W.F.)

* Correspondence: victoria.suponitsky@generalfusion.com or luna_ind2002@yahoo.com; Tel.: +1-778-3026412

† These authors contributed equally to this work.

Abstract

Electromagnetic implosions of hollow lithium cylinders can be utilized to compress magnetized plasma targets in the context of Magnetized Target Fusion (MTF). Two small-scale experiments were conducted at General Fusion as a stepping stone toward compressing magnetized plasmas on a larger scale. The first experiment is an electromagnetic implosion of a lithium ring, and the second is a compression of toroidal magnetic flux by imploding a hollow lithium cylinder onto an hourglass-shaped central structure. Here we present the methodology and results of modelling these experiments with OpenFOAM. Our in-house axisymmetric compressible MHD multi-phase solver was further extended to incorporate: (i) external RLC circuit model for electromagnetic compression coils and (ii) diffusion of the magnetic field into multiple solid materials. The implementation of the external RLC circuit model for electromagnetic coils was verified by comparison with results obtained with FEMM software and with the analytical solution. The solver was then applied to model both experiments and the main conclusions are as follows: (i) modelling solid lithium as a high-viscosity liquid is an adequate approach for the problems considered; (ii) the magnetic diffusivity of lithium is an important parameter for the accurate prediction of implosion trajectories (for the implosion of the lithium ring, higher values of magnetic diffusivity in the range $0.2 \leq \eta_{\mathrm{ring}}[\mathrm{m}^2/\mathrm{s}] \leq 0.5$ resulted in a better fit to the experimental data with a relative deviation in the trajectory of $\lesssim 20\%$); (iii) simulation results agree well with experimental data, and in particular, the toroidal field amplification of 2.25 observed in the experiment is reproduced in simulations within a relative error margin of 20%. The solver is proven to be robust and has the potential to be employed in a variety of applications.

Keywords: electromagnetic compression; MHD; multi-phase; RLC circuit; OpenFOAM; liner implosion; magnetic flux trapping; lithium

check for updates

Academic Editor: T. Hoehne

Received: 18 June 2025
Revised: 11 August 2025
Accepted: 19 August 2025
Published: 25 August 2025

Citation: Suponitsky, V.; Khalzov, I.V.; Roberts, D.M.; Forysinski, P.W. Compressing Magnetic Fields by the Electromagnetic Implosion of a Hollow Lithium Cylinder: Experimental Test Beds Simulated with OpenFOAM. *Fluids* **2025**, *10*, 222. https://doi.org/10.3390/fluids10090222

Copyright: © 2025 by the authors. Licensee MDPI, Basel, Switzerland. This article is an open access article distributed under the terms and conditions of the Creative Commons Attribution (CC BY) license (https://creativecommons.org/licenses/by/4.0/).

1. Introduction

The motivation behind this work is the ongoing development of Magnetized Target Fusion (MTF) at General Fusion which takes its origin from the LINUS concept [1,2]. The basic concept of MTF is to form a magnetized plasma target inside a conductive liner (flux conserver), which is then rapidly imploded to compress the plasma to fusion conditions [3–5]. Magnetized plasma targets, the geometry and physical state of the flux conserver (solid, liquid), and the liner implosion method may vary, with some being more suitable for concept demonstration, and others for power plant design [5–12]. A recent

paper by Turchi [13] provides an overview of the progress and issues with MTF, while a summary of the general progress in fusion energy can be found in [14].

Lawson Machine 26 (LM26) for MTF demonstration was recently commissioned at General Fusion. LM26 aims to demonstrate the heating of magnetized plasmas as they are compressed by the electromagnetically imploded, initially cylindrical, solid lithium liner [15]. A schematic (rz cross-section) of LM26 is shown in Figure 1. Here, a magnetized plasma target is injected into a vacuum cavity by the plasma injector (also known as a Marshall gun) as shown by the black arrow. The volume occupied by the plasma is constrained on the inside by the solid hourglass-shaped central structure (often referred to as the "centre shaft" in the manuscript) and by the lithium liner (shown by the cyan rectangle) on the outside. The vacuum boundary behind the liner is established by a cylindrical fibreglass vessel shown by the green rectangle. To shape the initial plasma and to prevent it from touching components of the machine on the liner side, a background poloidal magnetic field is generated inside the apparatus prior to the injection of the plasma. An example of such a field is shown by the blue contours on the right-hand side of the figure. The electromagnetic compression coil assembly (shown by the yellow rectangles) powered by a high-voltage capacitor bank causes the liner to implode, compressing the magnetized plasma. A typical trajectory of the inner surface of the liner during the implosion, along with the final shape of the compressed plasma, is shown on the left side of the figure.

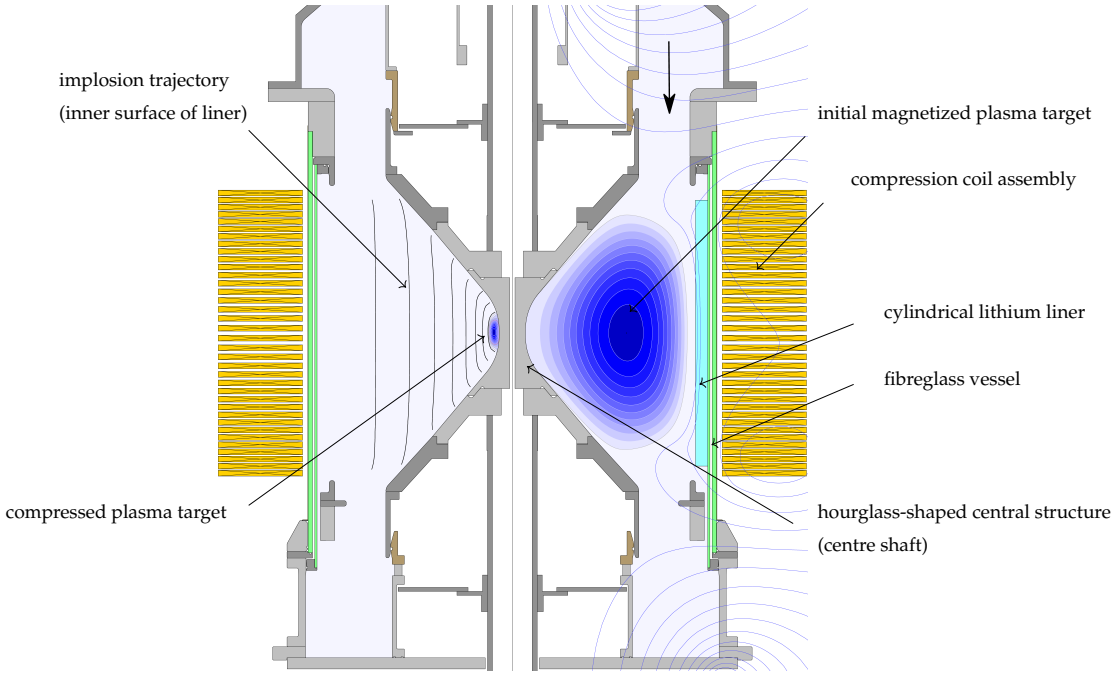


Figure 1. Schematic of LM26. The magnetized plasma target is injected into a vacuum cavity bounded on the inside by the hourglass-shaped central structure (centre shaft) and by the lithium liner on the outside. The injection path, indicated by the black arrow, and the magnetized plasma target are shown on the right side of the figure. An example of the background poloidal magnetic field prior to plasma injection is illustrated by the blue contours. The implosion trajectory and the compressed magnetized plasma target are shown on the left side of the figure.

To assist the LM26 experimental campaign, and the small-scale test beds used in its development, we would like to have simulation capability to model the entire system starting from the point plasma is injected into the vacuum cavity. To achieve this, the following are required: (i) the implementation of electromagnetic coils driven by an external RLC circuit, (ii) the incorporation of a multi-material solid structure to account for magnetic

field diffusion into solid parts, (iii) a plasma model and a means of differentiating between vacuum and plasma regions, and (iv) an adequate material model for the liner.

Given our extensive experience using the open-source OpenFOAM [16] software to model various compression schemes for MTF machines with liquid metal liners [11,17–20], including the development of an MHD axisymmetric solver [20], it is appealing to adapt our existing infrastructure to simulate the electromagnetic implosion of highly deformable solid lithium liners in the LM26 machine. A long term objective is to have a single open-source solver capable of simulating different ways to implode liquid or solid metal liners (pneumatic pistons, electromagnetic) to compress magnetized plasmas. Once the infrastructure is in place, more sophisticated plasma and material models can be incorporated. In the larger OpenFOAM community, the successful development of MHD implementations in other forms [21–26] suggests this is a fruitful path for further development of whole-device multiphysics simulations of MTF machines.

We now build upon our previous work [20] with focus on the implementation, verification, and validation of a model of electromagnetic compression coils driven by an external power supply. We also present a detailed description of a novel numerical algorithm for the self-consistent time evolution of an external RLC circuit coupled with axisymmetric compression coils. Two experimental test beds are then modelled and the results are compared with available experimental data. It is important to emphasize that the implementation of electromagnetic coils and the external RLC circuit model, as well as the incorporation of multiple rigid solids to simulate magnetic diffusion, are general and can be used with other solvers depending on the application of interest. The material model for the lithium liner is greatly simplified and the implementation of more sophisticated models is left to future work. Modelling of the entire LM26 machine including evolution of the magnetized plasma during compression is ongoing and results will be reported elsewhere.

The rest of the paper is organized as follows. The methodology, implementation, and verification of the electromagnetic coils and the external RLC circuit model are presented in Section 2. The results are presented in Section 3, which is divided into two parts: Section 3.1, in which an experiment of the electromagnetic implosion of a lithium ring in air is simulated and results are compared to experimental data, and Section 3.2, in which an experiment of the electromagnetic implosion of a hollow lithium cylinder onto an hourglass-shaped central structure compressing toroidal magnetic flux under vacuum is simulated and results are compared to experimental data. Lastly, a summary and conclusions are provided in Section 4.

2. Methodology

2.1. Governing Equations

This work is an extension of Suponitsky et al. [20], in which an axisymmetric two-phase compressible MHD solver ("mhdCompressibleInterFoam") was developed based on the standard compressible two-phase OpenFOAM solver "compressibleInterFoam". The MHD solver was developed with the OpenFOAM 10 version provided by "The OpenFOAM Foundation" [16] which we continue to use here. The MHD equations that were added to the standard "compressibleInterFoam" solver are shown below for convenient reference (Equations (3)–(5)). The complete set of governing equations for the "mhdCompressibleInterFoam" solver is provided in Appendix A along with some implementation details. A detailed description of the "mhdCompressibleInterFoam" solver can be found in [20].

In the axisymmetric case, the poloidal–toroidal decomposition of the magnetic field **B** [27–29] can be used (Equation (1)):

$$\mathbf{B} = \nabla\psi \times \nabla\phi + F\nabla\phi. \tag{1}$$

This reduces the induction equation given by Equation (2),

$$\frac{\partial \mathbf{B}}{\partial t} = \eta\nabla^2\mathbf{B} + \nabla \times (\mathbf{v} \times \mathbf{B}), \tag{2}$$

to two scalar equations for the toroidal function F (Equation (3)) and the poloidal flux per radian ψ (Equation (4)):

$$\frac{1}{r^2}\frac{\partial F}{\partial t} + \left[\nabla \cdot \left(\frac{\mathbf{v}}{r^2}F\right) - \nabla \cdot \left(\frac{\eta}{r^2}\nabla F\right)\right] - \nabla \cdot \left(\omega \mathbf{B}_{\text{pol}}\right) = 0, \tag{3}$$

$$\frac{\partial \psi}{\partial t} + \mathbf{v} \cdot \nabla\psi - \eta\left[r^2\nabla \cdot \left(\frac{1}{r^2}\nabla\psi\right)\right] = 0, \tag{4}$$

where $\eta[\text{m}^2/\text{s}]$ is the magnetic diffusivity, $\mathbf{v}$ is the velocity, $\omega = v_\phi/r$ is the angular velocity, $\mathbf{B}_{\text{pol}} = \nabla\psi \times \nabla\phi$ is a poloidal component of the magnetic field, and the cylindrical coordinate system (r, ϕ, z) is used. Note that magnetic diffusivity η is related to the electrical resistivity $\eta^{'}$ as $\eta = \eta^{'}/\mu_o$, where μ_o is the vacuum permeability.

Lorentz force is added as a source term to the momentum equation and is expressed through toroidal function F and poloidal flux per radian ψ as in Equation (5):

$$\begin{gathered}\text{Lorentz force}\left[\frac{\text{N}}{\text{m}^3}\right] = -\frac{\nabla\left(F^2\right)}{2\mu_o r^2} - \frac{1}{\mu_o r^2}\Delta^*\psi\nabla\psi + \frac{1}{\mu_o}\left(\mathbf{B}_{\text{pol}} \cdot \nabla F\right)\nabla\phi, \\ \text{where } \Delta^*\psi = r^2\nabla \cdot \left(\frac{1}{r^2}\nabla\psi\right).\end{gathered} \tag{5}$$

2.2. Modelling Electromagnetic Coils in OpenFOAM

2.2.1. Implementation of the Electromagnetic Coils Model

Conceptually, the idea is to use the equation for the poloidal flux function ψ (Equation (4)), which is already implemented in the "mhdCompressibleInterFoam" solver, to describe the evolution of magnetic fields in vacuum. With this approach, the vacuum is modelled as a resistive medium by setting a large, but finite, value for the magnetic diffusivity η_{vac} and it is set as a gas phase in the solver. The specific value of η_{vac}, which is required to adequately simulate the dynamics of magnetic fields in vacuum, may vary from one problem to another, as it depends on the size of the computational domain and the time scale of interest. The time and length scales of diffusion are related as $L \propto \sqrt{\eta_{\text{vac}}\Delta t_{\text{vac}}}$ and, therefore, the required value of η_{vac} increases with increasing size of the computational domain and shorter time scales.

In the current implementation, the electromagnetic compression coil has the shape of an axisymmetric toroid with a rectangular cross-section and is assumed to be a perfect conductor, i.e., there is no diffusion of magnetic field into the coil. As such, the poloidal flux remains spatially uniform over the cross-section of the coil, so the grid cells comprising the coil have the same value of $\psi_{\text{coil}}(t)$. This assumption is valid for high-frequency alternating current (AC), as penetration of the magnetic field (skin depth) is small (skin depth $\delta \propto \sqrt{\eta'/(f\mu)}$, where η' is electrical resistivity, f is current frequency and μ is magnetic permeability). The accuracy of this approximation for DC current depends on the problem in question. The poloidal flux is assumed to be zero at all boundaries of the

computational domain $\psi|_\Gamma = 0$, and the size of the domain is sufficient to minimize the effect of the boundary condition on the solution.

The computational mesh is conformed to the coil geometry, i.e., each grid cell lies either entirely inside or entirely outside the coil. As such, each coil is represented by a dedicated set of mesh cells within the computational domain. With the assumption of a perfect conductor, the poloidal flux remains spatially uniform across the surface of the coil. To apply time-varying voltage $V_{\text{coil}}(t)$ to the coil, the poloidal flux $\psi_{\text{coil}}(t)$ can be prescribed over the set of cells comprising the coil such that $d\psi_{\text{coil}}(t)/dt \propto V_{\text{coil}}(t)$.

It is worth mentioning that in our MHD description, at each moment in time there is a general relation between the poloidal flux of any coil $\psi_{\text{coil}}(t)$ and its total electric current $I_{coil}(t)$, derived from Ampère's circuital law, Equation (6) (the exact procedure is detailed later in this section):

$$\mu_0 N I_{\text{coil}}(t) = \oint_{\mathcal{C}} \mathbf{B}_{\text{pol}}(t) \cdot d\mathbf{l}, \tag{6}$$

where integration contour $\mathcal{C}$ is a closed curve around the coil oriented clockwise, and N is the number of turns in the coil. In the simple case of the single-turn stationary perfectly conducting coil considered here, this relation can be expressed as Equation (7) (assuming the vacuum diffusion time scale Δt_{vac} is negligible compared to the dynamic time scales of interest):

$$\Psi_{\text{coil}}(t) \equiv 2\pi\psi_{\text{coil}}(t) = L_{\text{coil}} I_{\text{coil}}(t), \tag{7}$$

where L_{coil} is the time-constant coil inductance determined solely by the geometry of the coil and the computational domain. In this case, clockwise orientation of the integration contour $\mathcal{C}$ in Equation (6) ensures that I_{coil} is positive (flowing into the page) when ψ_{coil} is positive, and therefore L_{coil} is also positive.

2.2.2. Verification of the Electromagnetic Coils Model

To demonstrate and verify this implementation, the test problem of a single coil placed inside a hollow cylindrical vacuum void with perfect conductor walls is modelled with both OpenFOAM and FEMM (Finite Element Method Magnetic, version 4.2) software [30]. The size of the computational domain and the boundary conditions are identical in both codes. The radial and axial extents of the computational domain are $0.1 \leq r[\text{m}] \leq 0.4$ and $-0.2 \leq z[\text{m}] \leq 0.2$, respectively. The geometry of the coils and the parameters are given in Table 1. In OpenFOAM, the computational domain is a one-cell-thick wedge (5°), which is a standard way to simulate two-dimensional axisymmetric problems in OpenFOAM [16,31]. A uniform structured orthogonal mesh is used with 1 mm resolution in both the radial and axial directions. The vacuum grid cells are initialized with $\psi = 0$, and for the grid cells comprising the coil, a constant value of $\psi_{\text{coil}}(t) = \psi_{0\,\text{coil}}$ is prescribed. The system is then evolved until a steady state is reached.

In FEMM simulations, an automatically generated triangular mesh is used as shown in Figure A1. The amplitude of the electric current in the coil (required input in FEMM) is set to the value obtained in the OpenFOAM simulation, calculated using Equation (6), as in Table 1. In FEMM, magnetic diffusion into the coil is taken into account. This allows us to see how the magnetic field outside the coil differs from that when the coil is assumed to be a perfect conductor, as in OpenFOAM. The coil material is set to copper and simulations are performed for three frequencies of AC current to vary the skin depth. Note that although the OpenFOAM results correspond to steady state (DC) cases, their comparison with the FEMM AC cases is still mathematically valid in terms of the amplitudes of the obtained fields. The comparison between OpenFOAM and FEMM is given in Figure 2. Part (a) shows the steady-state solution obtained with OpenFOAM for a perfect conductor coil. Parts (b), (c), and (d) correspond to FEMM results obtained with different frequencies of electric

current $f = 1 \times 10^6$ Hz, $f = 1 \times 10^3$ Hz, and $f = 0$ (DC), respectively. In Figure 2, the magnitude of the magnetic field **B** is shown by the colour map and the contours correspond to the poloidal flux Ψ; the colour map and contours are shown for the same range of values for both codes. Values of Ψ_{coil}, I_{coil}, and L_{coil} are given in Table 1. The inductance L_{coil} is calculated by Equation (7).

Table 1. Parameters for DC coil verification case.

Test	Coil Geometry	Parameters [1]
One coil	$0.2 \leq r[\text{m}] \leq 0.3$; $0.01 \leq z[\text{m}] \leq 0.05$	$\Psi_{\text{coil}} = 0.125$ Wb, $I_{\text{coil}} = 290,310$ A, $L_{\text{coil}} = 430$ nH

[1] Simulations were run for several values of vacuum magnetic diffusivity η_{vac}. Nominal $\eta_{\text{vac}} = 10^5$ m^2/s.

One can see that the results obtained with OpenFOAM are very similar to those obtained with FEMM for high-frequency current, when there is very little penetration of the magnetic field into the coil (compare Figure 2a and 2b). When comparing FEMM solutions for $f = 10^6$ Hz and $f = 10^3$ Hz, the magnetic fields outside the coils are very similar, even though there is some penetration of the field into the coil for $f = 10^3$ Hz. In the DC current scenario, the magnetic field is fully diffused through the coil and some changes to the magnetic field structure around the coil can be observed.

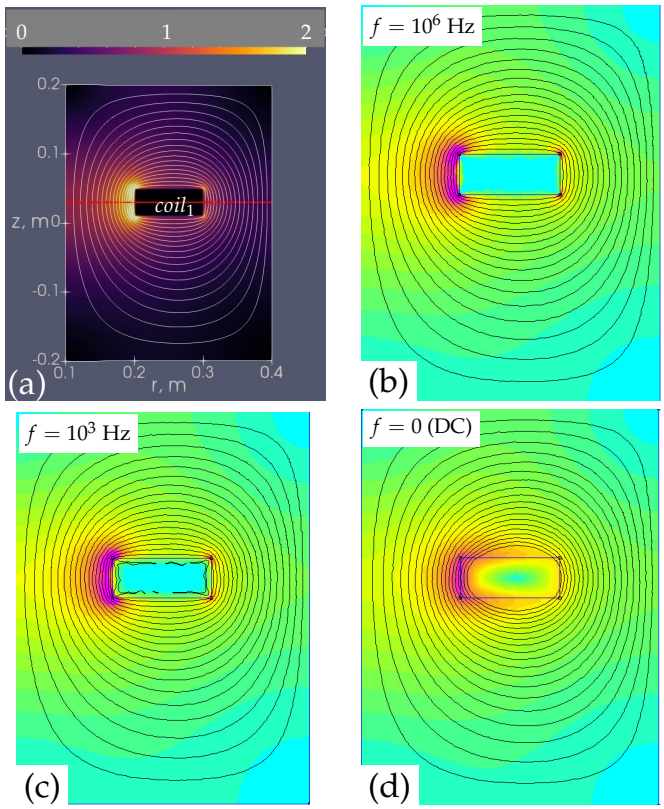


Figure 2. Comparison between OpenFOAM and FEMM results for a single magnetic coil in a vacuum void. The geometry of the coil and the simulation parameters are given in Table 1. (**a**) OpenFOAM results. Steady state solution obtained by prescribing constant values of the poloidal flux $\Psi = \Psi_{\text{coil}}$ for sets of mesh cells that comprise coils (ideal conductor). FEMM results for three frequencies of electric current: (**b**) $f = 10^6$ Hz; (**c**) $f = 10^3$ Hz; and (**d**) $f = 0$ (DC). The coil material was set to copper, and diffusion of the magnetic field was accounted for. The colour map shows the magnitude of the magnetic field **B** ($0 \leq |\mathbf{B}| \leq 2$ T). Also shown are the contours of the poloidal flux Ψ within the range $0 \leq \Psi \leq 0.125$ Wb, $\Delta\Psi = 0.007$ Wb (19 contours). Range and contour values are identical for OpenFOAM and FEMM.

The radial profiles of the poloidal flux Ψ at the axial position aligned with the middle of the coil (as shown by the red line in Figure 2a) for the four simulations in Figure 2 are shown in Figure 3. OpenFOAM results are plotted with a black line. FEMM results are shown using red lines, with solid, dash-dot and dashed lines corresponding to AC current with frequencies $f = 10^6$ Hz, $f = 10^3$ Hz, and $f = 0$ (DC), respectively. One can see that for high-frequency AC current, the distribution of the poloidal flux Ψ outside the coil is almost identical in OpenFOAM and FEMM. For DC current, the distribution of Ψ outside the coil is also not greatly dissimilar from that obtained with high-frequency AC current, despite the magnetic field being fully diffused into the coil. Resolution and domain size checks were performed for both codes to ensure convergence of the results.

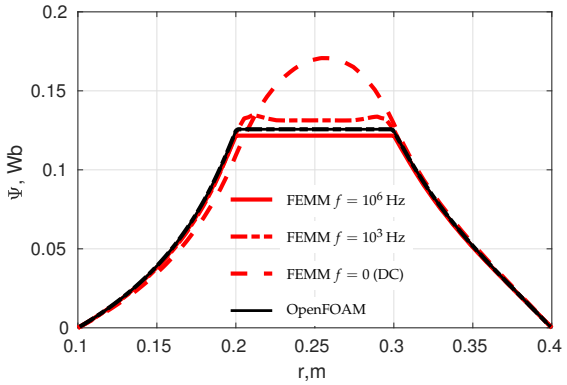


Figure 3. Comparison between OpenFOAM and FEMM. Radial Ψ profile at the mid-plane of the coil (along the red line in Figure 2a): OpenFOAM results are shown using the solid black line, $\eta_{\text{vac}} = 10^5$ m^2/s. FEMM results are shown with red lines for three cases: (i) solid line—AC current with $f = 10^6$ Hz; (ii) dash-dot line—AC current with $f = 10^3$ Hz; and (iii) dashed line—DC current $f = 0$.

2.3. Modelling the External RLC Circuit in OpenFOAM

2.3.1. Implementation of the External RLC Circuit Model

A schematic of the electromagnetic coil connected to the external circuit as implemented in OpenFOAM is shown in Figure 4. It is assumed that an experimental circuit comprising high-voltage capacitors, inductors, and cables can be reduced to the theoretical equivalent RLC circuit using effective parameters R_{eff}, L_{eff}, and C_{eff} as shown in Figure 4a. The experimental circuit also features a diode, so the RLC circuit model is extended to include a diode (ideal), as shown in Figure 4b. All the external inductive and resistive components are combined into two sets L_{cap}, R_{cap} and L_{cable}, R_{cable}. The diode is turned on or off depending on the voltage across it. Initially, the diode is turned off with $V_{\text{diode}} > 0$ and the voltage applied to the coil, V_{coil}, is governed by the green loop (Figure 4b). When the voltage across the diode becomes negative ($V_{\text{diode}} < 0$), the diode is turned on, and the voltage applied to the coil is dictated by the cyan loop. Also shown in Figure 4 is the set of cells encircling the coil (dark grey colour). This set of cells is used to evaluate the current in the coil (using Equation (6), with the integration path shown by the yellow line). For the problems considered, the initial condition of the external circuit is a capacitor bank charged to a target voltage which begins to discharge at $t = 0$ to power the compression coil.

To apply a time-dependent voltage to the coil, the poloidal flux as a function of time should be specified for the cells comprising the coil. Poloidal flux $\psi_{\text{coil}}(t)$ is calculated using the parameters of the external circuit and the procedure is detailed below. For the coil connected to an equivalent RLC circuit, Kirchhoff's second law (loop rule) can be written as follows (Equation (8)):

$$V_{\text{coil}} = V_C + V_L + V_R, \tag{8}$$

where V_{coil}, V_c, V_L, and V_R are the voltage drops across the coil, capacitor, inductive, and resistive components, respectively. The voltage drops across different components in Equation (8) are calculated using Equation (9):

$$V_{\text{coil}} = -2\pi N \frac{d\psi_{\text{coil}}}{dt}, \; V_c = \frac{Q}{C_{\text{eff}}}, \; V_L = L_{\text{eff}} \frac{dI_{\text{coil}}}{dt}, \; V_R = R_{\text{eff}} I_{\text{coil}}, \tag{9}$$

where N is the number of turns in the coil, Q is the electric charge of the capacitor, and I_{coil} is the electric current in the coil. After substituting Equation (9) into Equation (8) and rearranging terms, the equation for the total flux Φ is obtained (Equation (10)):

$$\frac{d\Phi}{dt} = -\underbrace{\left[\frac{Q}{C_{\text{eff}}} + R_{\text{eff}} I_{\text{coil}}\right]}_{\text{rhs}}, \text{ where } \Phi = 2\pi N \psi_{\text{coil}} + L_{\text{eff}} I_{\text{coil}} \text{ and } \frac{dQ}{dt} = I_{\text{coil}}. \tag{10}$$

This system of circuit equations should be supplemented with the relation between the electric current I_{coil} passing through the coil and the value of the poloidal flux at the coil ψ_{coil}, which is obtained from Ampére's law, given by Equation (6) (we rewrite it below for convenience). In the present implementation, the line integral in Equation (11) is calculated along the closed curve shown by the yellow line in Figure 4.

$$\mu_o \, N \, I_{\text{coil}} = \oint_C \mathbf{B}_{\text{pol}} \cdot d\mathbf{l}, \quad \text{Ampére's law.} \tag{11}$$

In the calculation of the line integral in Equation (11), only the poloidal component of the magnetic field is used. The poloidal magnetic field is related to the poloidal flux ψ as:

$$\mathbf{B}_{\text{pol}} = \nabla\psi \times \nabla\phi, \tag{12}$$

where ϕ is azimuthal angle.

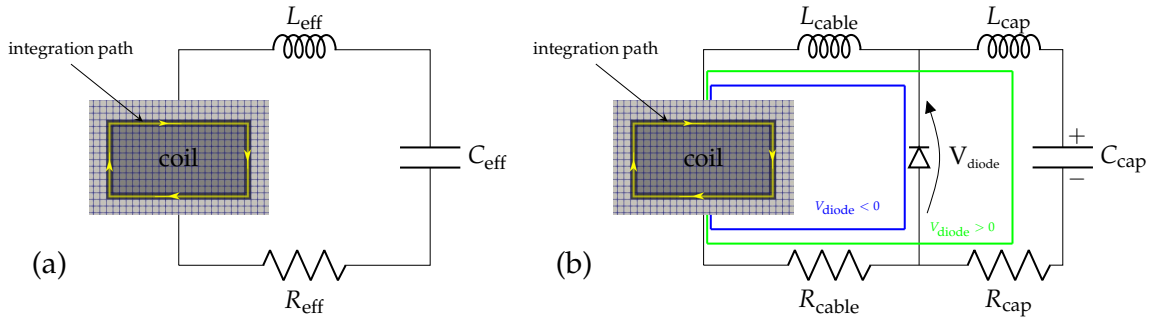


Figure 4. A schematic of the electromagnetic compression coil connected to the external circuit. The coil is represented by a set of grid cells. The poloidal flux ψ_{coil} for this set of cells is calculated from the voltage applied to the coil by the external RLC circuit. (**a**) External circuit reduced to the theoretical equivalent RLC circuit. L_{eff}, R_{eff}, and C_{eff} are the effective values of the equivalent circuit. (**b**) Variation of the basic circuit which includes an ideal diode. The diode turns on or off depending on the sign of the voltage across it. Initially ($t = 0$) the coil is connected to the green loop (positive voltage across the diode) and switches to the blue loop when the diode turns on (voltage across the diode becomes negative). Effective values are then calculated using the appropriate current loop determined by the voltage across the diode. Grid cells encompassing the coil (marked by the dark grey colour) are used to calculate the contour integrals required for the circuit model.

A scalar poloidal flux field ψ is then decomposed into two fields ψ_1 and $\psi_{\text{coil}}\hat{\psi}_0$, as in Equation (13):

$$\mathbf{B}_{\text{pol}} = \nabla\psi \times \nabla\phi = \nabla\left[\psi_1 + \psi_{\text{coil}}\hat{\psi}_0\right] \times \nabla\phi = \underbrace{\nabla\psi_1 \times \nabla\phi}_{\mathbf{B}_1} + \psi_{\text{coil}}\underbrace{\nabla\hat{\psi}_0 \times \nabla\phi}_{\hat{\mathbf{B}}_0}, \tag{13}$$

where corresponding fields ψ_1 and $\psi_{\text{coil}}\hat{\psi}_0$ are shown in Figure 5. This results in splitting the line integral in Equation (6) into two parts, using fields $\mathbf{B}_1$ and $\hat{\mathbf{B}}_0$ as written in Equation (14):

$$\mu_0 N I_{\text{coil}}(t) = \oint_{\mathcal{C}} \mathbf{B}_{\text{pol}} \cdot d\mathbf{l} = C_1(t) + \psi_{\text{coil}}(t)\, C_0;\ C_1(t) = \oint_{\mathcal{C}} \mathbf{B}_1(t) \cdot d\mathbf{l} \text{ and } C_0 = \oint_{\mathcal{C}} \hat{\mathbf{B}}_0 \cdot d\mathbf{l}, \tag{14}$$

which directly relates the current I_{coil} to the poloidal flux ψ_{coil}. It should be noted that in Equation (14), C_0 is a constant defined by the geometry of the coil and is calculated once at the beginning of the simulation, while C_1 needs to be recalculated at each time step based on the distribution of ψ_1. Equations (4), (10), and (14) constitute a circuit model for the electromagnetic compression coil connected to the basic equivalent RLC circuit.

As a result, we implement a novel numerical algorithm for the self-consistent coupled time evolution of the electromagnetic compression coil and the external RLC circuit. This algorithm is summarized below.

1. At the beginning of the simulation, calculate the value C_0 in Equation (14) using the vector field $\hat{\mathbf{B}}_0$ (Equation (13), Figure 5). At $t = 0$, set the initial poloidal flux distribution in the domain to $\psi^0 = 0$ (including $\psi^0_{\text{coil}} = 0$ at the coil), current $I^0_{\text{coil}} = 0$, full flux $\Phi^0 = 0$, and the capacitor charge $Q^0 = C_{\text{eff}} V_0$ based on the initial capacitor voltage V_0.

At each time step $t = t_n$, the scalar field ψ^n and the values of Φ^n and Q^n are known. Then, do the following:

2. Calculate the value C^n_1 in Equation (14) using the vector field $\mathbf{B}^n_1$ with mesh values of ψ^n_1 (Equation (13), Figure 5).
3. Calculate values for ψ^n_{coil} and I^n_{coil} from the total flux Φ^n (Equation (10)) and Ampère's circuital law (Equation (14)) as:

$$\begin{cases} \psi^n_{\text{coil}} &= \left[\Phi^n - \frac{L_{\text{eff}}\, C^n_1}{\mu_0\, N}\right] / \left[2\pi N + \frac{L_{\text{eff}} C_0}{\mu_0 N}\right] \\ I^n_{\text{coil}} &= \frac{1}{\mu_0 N}\left[C^n_1 + \psi^n_{\text{coil}}\, C_0\right] \end{cases} \tag{15}$$

4. Assign the updated value of ψ^n_{coil} to the mesh cells comprising the coil.
5. Advance in time the poloidal flux scalar field ψ in vacuum using Equation (4), with vacuum resistivity η:

$$\psi^{n+1} = \psi^n + dt[-\mathbf{v} \cdot \nabla\psi^n + \eta\, \Delta^*\psi^n] \tag{16}$$

6. Advance in time the total flux Φ using Equation (10) as:

$$\Phi^{n+1} = \Phi^n - dt\left[\frac{Q^n}{C_{\text{eff}}} + R_{\text{eff}} I^n_{\text{coil}}\right] \tag{17}$$

7. Advance in time the electric charge of the capacitor bank using Equation (18):

$$Q^{n+1} = Q^n + dt\, I^n_{\text{coil}}. \tag{18}$$

8. Go to 1 at the next time step.

The equations and the implementation are also valid for a modified circuit which includes the diode, which switches between the green and blue loops in Figure 4b depending on the voltage across it. For the circuit with the diode, there is an additional step of calculating the voltage across the diode. This is required to identify the electric loop connected to the electromagnetic coil (Figure 4b). The corresponding effective values of inductance L_{eff} and resistance R_{eff} are then calculated. These values are subsequently utilized in the circuit model equations. Lastly, it is worth noting that the second part in Equation (15) can be rearranged to directly calculate the value of ψ_{coil}, if the value of I_{coil} is known. This can be useful in certain scenarios. For example, if there are experimental measurements of the current, these can be applied directly to calculate ψ_{coil} to drive the electromagnetic coil. This trick can also be used to model a coil that is physically present in the setup but is not connected to the circuit, as this scenario can be approximated by enforcing zero toroidal current in the coil during the simulation.

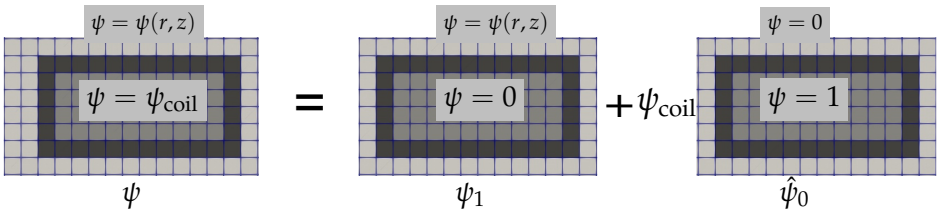


Figure 5. Decomposition of the poloidal flux field ψ for the implementation of the circuit model. Dark grey cells constitute the integration path for the line integral in Equation (6). At each time step, the poloidal flux field $\psi = \psi(r,z)$ is reset to $\psi = \psi_{\text{coil}}$ for cells comprising the coil. For the line integral calculation, the poloidal flux is decomposed into two parts: (1) field ψ_1: $\psi_1 = 0$ is set for the coil cells and $\psi_1 = \psi(r,z)$ outside, and (2) field $\psi_{\text{coil}}\hat{\psi}_0$: $\hat{\psi}_0 = 1$ for the coil cells and $\hat{\psi}_0 = 0$ outside. As the value of ψ_{coil} is the same for all cells comprising the coil, it can be taken outside as a constant multiplier in front of $\hat{\psi}_0$.

2.3.2. Verification Tests of the RLC Circuit Model

The implementation of the circuit model is verified using a test case of a single coil in a vacuum cavity (enclosed by a perfect conductor) connected to the external circuit as shown in Figure 4. The simulation setup is the same as for the single-coil implementation test shown in Figure 2a. Verification is carried out by comparing the electric current I_{coil} calculated in the OpenFOAM simulation to that obtained analytically for the same set of parameters, i.e., the same effective resistance, inductance, capacitance, and initial capacitor voltage. In calculating the parameters of the analytical circuit, one should note that the resistance and capacitance of the circuit are explicitly specified parameters of the OpenFOAM external circuit model, whereas the effective inductance is an implicit result of the domain and geometry of the simulation. Here, since we are using the same setup as in the coil test discussed above, the inductance of the coil has already been calculated and is equal to $L_{\text{coil}} = 430\,\text{nH}$ (as listed in Table 1). This value is used to calculate the effective inductance used in the analytical solution for comparison with OpenFOAM. For the initial conditions given by Equation (19), the electric current in the RLC circuit is given by Equation (20). More details about the analytical solution can be found in Appendix B.

$$I(t=0) = 0 \text{ and } Q(t=0) = V_o\, C_{\text{eff}}. \tag{19}$$

$$\begin{aligned} I(t) &= -\frac{\beta^2 + \omega_d^2}{\omega_d}\, V_o\, C_{\text{eff}}\, e^{-\beta t}\, \sin(\omega_d\, t), \text{ where} \\ \omega_d &= \sqrt{\omega_0^2 - \beta^2},\ \beta = \frac{R_{\text{eff}}}{2L_{\text{eff}}},\ \omega_0 = \frac{1}{\sqrt{L_{\text{eff}} C_{\text{eff}}}}. \end{aligned} \tag{20}$$

For a circuit that includes a diode, when the diode is on, the RLC circuit switches to an RL circuit, with the corresponding electric current given by Equation (21).

$$I(t > t_d) = I_d e^{-R_{\text{eff}}(t-t_d)/L_{\text{eff}}}, \tag{21}$$

where t_d is the time when the diode is activated, I_d is the value of the electric current when the diode is activated, and R_{eff} and L_{eff} are the effective resistance and inductance of the corresponding RL circuit (Figure 4b).

The comparison between OpenFOAM and the analytical solution is presented in Figure 6. Circuit parameters used in OpenFOAM simulations (see Figure 4b for circuit diagram) and corresponding effective parameters used in the analytical solution are listed in Table 2. OpenFOAM results obtained with nominal values for vacuum magnetic diffusivity and simulation time step ($\eta_{\text{vac}} = 10^5\,\text{m}^2/\text{s}$ and $\text{dt} = 10^{-8}\,\text{s}$) are shown by red lines for two cases: (i) solid red line—the diode is disconnected, and (ii) dash-dot red line—the diode is connected and turns on when the voltage across it becomes negative. The analytical solution given by Equation (20) with the parameters listed in Table 2 is shown by the solid black line. The analytical solution for the current decay in the RL circuit (Equation (21)) that describes the behaviour once the diode is turned on is shown by the dashed black line; values for the current I_d and time t_d are taken from the OpenFOAM simulation.

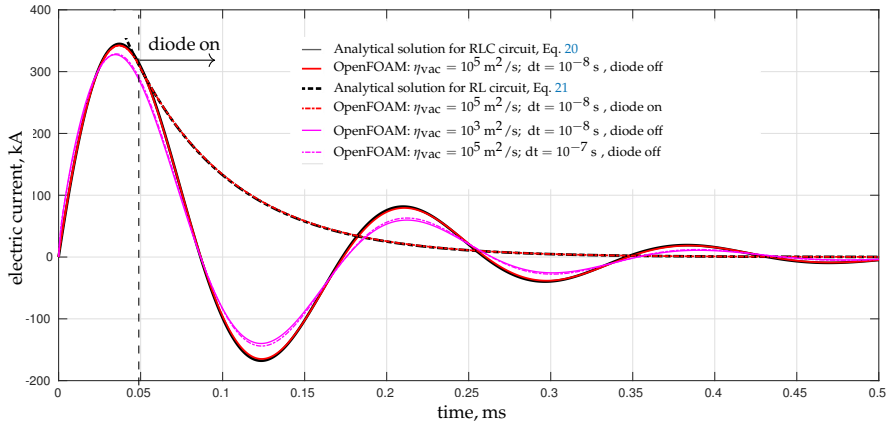


Figure 6. Comparison between the electric current calculated in OpenFOAM simulations of a single electromagnetic coil in a vacuum chamber connected to an external circuit and the analytical solution obtained for the same values of effective resistance, inductance, and capacitance. OpenFOAM results for the basic RLC circuit (without diode) are shown by the solid red ($\eta_{\text{vac}} = 10^5\,\text{m}^2/\text{s}$, $\text{dt} = 10^{-8}\,\text{s}$), solid magenta ($\eta_{\text{vac}} = 10^3\,\text{m}^2/\text{s}$, $\text{dt} = 10^{-8}\,\text{s}$), and dash-dot magenta ($\eta_{\text{vac}} = 10^3\,\text{m}^2/\text{s}$, $\text{dt} = 10^{-7}\,\text{s}$) lines. The corresponding analytical solution (Equation (20)) is shown by the solid black line. Electric current calculated for the circuit including a diode is shown by the red dash-dot line, with the analytical solution given by Equation (21) (valid from the moment the diode is activated) plotted with the dashed black line.

Two additional OpenFOAM simulations were carried out to study the sensitivity of the solution to the vacuum magnetic diffusivity and the time step. These are shown with magenta lines: (i) solid magenta line—the vacuum magnetic diffusivity value is reduced to $\eta_{\text{vac}} = 10^3\,\text{m}^2/\text{s}$ while keeping the nominal time step of $\text{dt} = 10^{-8}\,\text{s}$, and (ii) dash-dot magenta line for a larger time step $\text{dt} = 10^{-7}\,\text{s}$ and the nominal value of the vacuum magnetic diffusivity $\eta_{\text{vac}} = 10^5\,\text{m}^2/\text{s}$. One can see that for the nominal values of the vacuum magnetic diffusivity and time step, solutions obtained in OpenFOAM are in excellent agreement with the corresponding analytical solutions obtained for the same effective circuit parameters. It can also be seen that for the frequency considered in this

test, reducing the vacuum magnetic diffusivity by a factor of 100 or increasing the time step by a factor of 10 results in a noticeable difference between OpenFOAM and the analytical solution. This emphasizes the need to tune those parameters for the specific problem of interest, and the test problems provide an effective and reasonably rigorous way of guiding what values of those parameters are required for a given physical regime. The length and time scales used in the verification tests are similar to those in the problems we want to simulate. Therefore, in the simulations described in the "Results", Section 3, $\eta_{\text{vac}} = 10^5\,\text{m}^2/\text{s}$ and $\text{dt} = 10^{-8}\,\text{s}$ were chosen as the nominal values.

Table 2. Circuit parameters used in circuit implementation verification test (results are shown in Figure 6).

Test	Circuit Parameters
OpenFOAM [1]	$R_{\text{cap}} = 0,\ L_{\text{cap}} = 0,\ C = 1200\,\mu\text{F},\ V_o = -10.5\,\text{kV},$ $R_{\text{cable}} = 0.01\,\Omega,\ L_{\text{cable}} = 170\,\text{nH},\ L_{\text{coil}} = 430\,\text{nH}$ (not an input, calculated in simulation)
Analytical Equation (20)	Diode off: $R_{\text{eff}} = R_{\text{cap}} + R_{\text{cable}} = 0.01\,\Omega,$ $L_{\text{eff}} = L_{\text{cap}} + L_{\text{cable}} + L_{\text{coil}} = 600\,\text{nH},\ C_{\text{eff}} = 1200\,\mu\text{F},\ V_o = -10.5\,\text{kV}$ $\beta = 8333.3\,\text{rad/s},\ \omega_o = 37268\,\text{rad/s},\ \omega_d = 36324\,\text{rad/s}$
Analytical Equation (21) [2]	Diode on: $R_{\text{eff}} = R_{\text{cable}} = 0.01\,\Omega,$ $L_{\text{eff}} = L_{\text{cable}} + L_{\text{coil}} = 600\,\text{nH},\ I_d = 307378\,\text{A},\ t_d = 4.957 \times 10^{-5}\,\text{s}$

[1] Sketch of the circuit implemented in OpenFOAM with required parameters is shown in Figure 4b. [2] Values of I_d and t_d at time diode is turned on are taken from the OpenFOAM simulation.

3. Results

The "mhdCompressibleInterFoam" solver supplemented with the external RLC circuit model was used to simulate two experimental test beds. The first is an electromagnetic implosion of a solid lithium ring (Section 3.1), and the second is an electromagnetic implosion of a hollow lithium cylinder onto an hourglass-shaped central structure (Section 3.2).

3.1. Implosion of a Solid Lithium Ring

The primary objective is to assess how accurately the solver can predict the shape and trajectory of the imploding ring. In particular, we aim to determine whether modelling solid lithium as a high-viscosity liquid is adequate for the range of parameters used in the experiment.

3.1.1. Experimental Apparatus

The experimental electromagnetic compression system for the implosion of a solid lithium ring is shown in Figure 7. The compression coil assembly is constructed from individual 6.4 mm thick aluminum plates (turns) that are stacked on top of each other with insulating material between them (DMD100.3753, Electrowind). This design allows flexibility in tuning the magnetic field produced by the compression coil assembly by varying the number of plates, the electrical connection between plates, or the spacing between the plates. For this experiment, the compression coil assembly is composed of eight identical plates (turns), combined into two coils of four turns each. Within each coil, individual turns are electrically connected in series. Each of the two coils is connected to a bank of twenty four high-voltage capacitors (General Electric, 52 μF arranged in pairs) that can be charged up to 16 kV. A solid lithium ring is placed inside the compression coil assembly and concentrically aligned with it. The compression system is located inside a shipping container to minimize the hazards of working with lithium and flying debris. More details on the experimental apparatus and data collection can be found in [32].

During the discharge of the capacitors, electric current flows through the coil generating a magnetic field around it (like in a solenoid). This poloidal magnetic field then induces a toroidal electric current in a thin layer of material at the outer surface of the lithium ring. This results in a Lorentz force acting upon the lithium ring in an inward radial direction and causing the ring to implode. Images of the imploding lithium ring captured by a high-speed camera are shown in Figure 8. It can be seen that the lithium ring remains symmetric during the implosion and its inner surface remains smooth without obvious buckles. The parameters and data for this implosion of the lithium ring were used to compare with the numerical results.

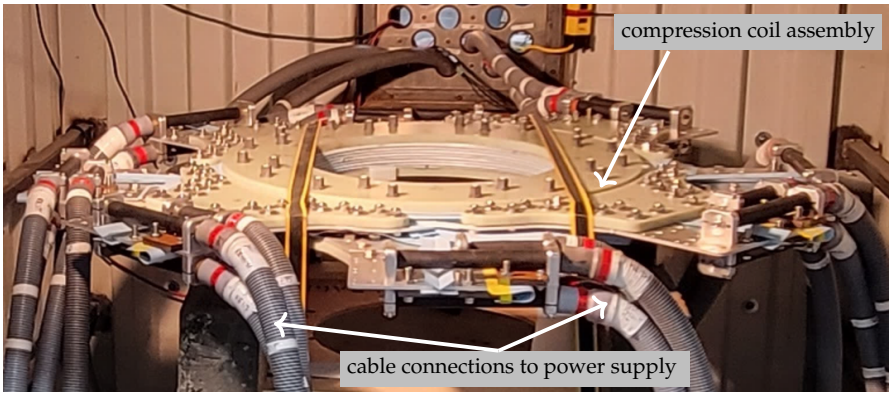


Figure 7. Experimental apparatus for electromagnetic implosion of a solid lithium ring built at General Fusion.

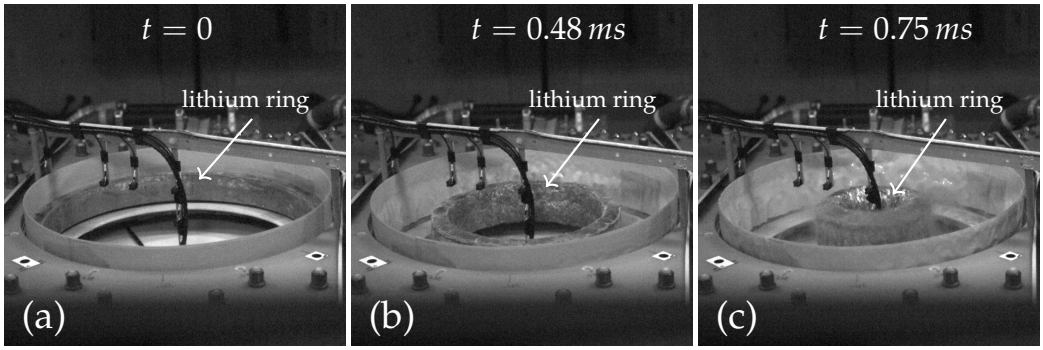


Figure 8. Snapshots of the lithium ring during the implosion captured by high-speed camera. The initial temperature of the lithium ring is 100 °C. (**a**) $t = 0$ (before implosion); (**b**) $t = 0.48$ ms; (**c**) $t = 0.75$ ms.

3.1.2. Numerical Setup and Implosion Dynamics

The numerical setup to simulate the implosion of a solid lithium ring is shown in Figure 9 (rz cross-section). To simulate two-dimensional axisymmetric problems in OpenFOAM, the geometry is specified as a wedge of small angle (5°) which is one cell thick and runs along the plane of symmetry. The front and back planes of the wedge are specified as separate patches and for each patch, the boundary condition is set to `wedge` type (see OpenFOAM documentation [16] and reference [31] for more details). The extent of the computational domain in the radial and axial (vertical) directions is $0.01 \leq r[\mathrm{m}] \leq 1.2$ and $-0.7 \leq z[\mathrm{m}] \leq 0.7$, respectively. The computational domain does not extend all the way to $r = 0$ to avoid singularity. The resolution of the initially uniform background mesh is $\Delta r = \Delta z = 2$ mm. The mesh has three levels of refinement and the resolution in the region of primary interest is 0.25 mm. Refined regions are shaded with different colours in Figure 9. (Refinement regions: $0.1 \leq r[\mathrm{m}] \leq 0.7$, $|z[\mathrm{m}]| \leq 0.1$; $0.7 \leq r[\mathrm{m}] \leq 0.8$, $0.1 \leq |z[\mathrm{m}]| \leq 0.2$;

$0.8 \leq r[\mathrm{m}] \leq 1, 0.2 \leq |z[\mathrm{m}]| \leq 0.5$.) This size of computational domain and mesh resolution were found to be sufficient to produce converged results for the problem in question.

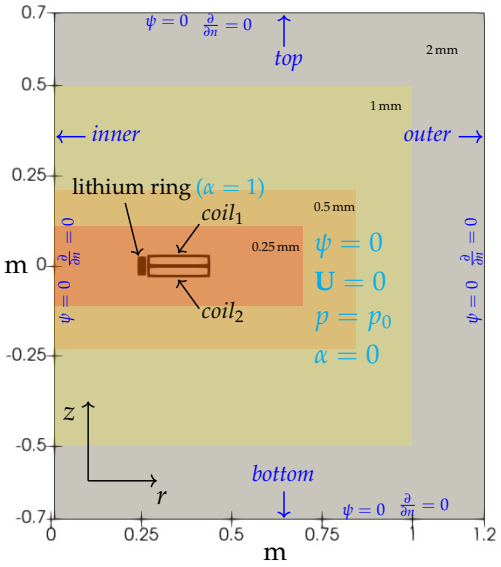


Figure 9. Computational setup (rz cross-section) used to simulate the experiment of an electromagnetically imploding lithium ring.

Following the experimental setup, the compression coil assembly comprises two separate coils (denoted $coil_1$ and $coil_2$), with four turns each. Each of the coils is connected to its own RLC circuit using effective parameters derived from the experimental circuit. The inner and outer radii of the coils are $R_{\mathrm{coil}_{\mathrm{inner}}} = 0.2695\,\mathrm{m}$ and $R_{\mathrm{coil}_{\mathrm{outer}}} = 0.437\,\mathrm{m}$, respectively. The height of the entire coil is $h_{\mathrm{coil}} = 0.057\,\mathrm{m}$ with a vacuum (gas phase) gap of 1 mm between the coils. The axial position is $0.0005 \leq z_{\mathrm{coil}_1}[\mathrm{m}] \leq 0.0285$ for $coil_1$ and $-0.0285 \leq z_{\mathrm{coil}_2}[\mathrm{m}] \leq -0.0005$ for $coil_2$. The effective circuit parameters used in the simulations presented in this section are as follows: $R_{\mathrm{cable}} = 0.01\,\Omega$, $R_{\mathrm{cap}} = 0.42 \times 10^{-3}\,\Omega$, $L_{\mathrm{cable}} = 800\,\mathrm{nH}$, $L_{\mathrm{cap}} = 33.3\,\mathrm{nH}$, $C_{\mathrm{cap}} = 1248\,\mu\mathrm{F}$, and $V_{\mathrm{cap}} = 12\,\mathrm{kV}$ (unless stated otherwise). The actual capacitor voltage in the experiment was 14 kV; the value used in the simulation was adjusted to match the value of the maximum electric current measured in the experiment. This is discussed later in this section. The same set of effective circuit parameters is used to drive each of the coils. The dimensions of the lithium ring correspond to those used in the experiment shown in Figure 8 with the inner and outer radii equal to $R_{\mathrm{ring}_{\mathrm{inner}}} = 0.239\,\mathrm{m}$ and $R_{\mathrm{ring}_{\mathrm{outer}}} = 0.264\,\mathrm{m}$ and the height of the ring (rectangular cross-section) $h_{\mathrm{ring}} = 0.054\,\mathrm{m}$ ($-0.027 \leq z_{\mathrm{ring}}[\mathrm{m}] \leq 0.027$). With this setup, the initial spacing between the outer surface of the lithium ring and the inner surface of the coil is 5.5 mm, which is resolved with 22 grid cells.

The volume fraction field is initially set to $\alpha = 1$ for the region occupied by the lithium ring, and to $\alpha = 0$ elsewhere in the domain. The initial velocity and poloidal flux fields are set to zero, and the pressure field is set to $p = p_o = 10^5\,\mathrm{Pa}$. At all boundaries of the computational domain, the poloidal flux is set to zero ($\psi = 0$), with a zero normal gradient boundary condition applied to the velocity, pressure, and volume fraction fields. The vacuum (air) region was modelled as an ideal gas. The magnetic diffusivity of the vacuum was set to $\eta_{\mathrm{vac}} = 10^5\,\mathrm{m}^2/\mathrm{s}$. Simulations were run with an adjustable time step, with an upper bound of $\mathrm{dt}_{\mathrm{max}} = 10^{-8}\,\mathrm{s}$.

In all simulations presented in this paper, solid lithium was modelled as a compressible fluid, and a barotropic equation of state given by Equation (22) (variation of Tait equation [33]) was used to account for compressibility.

$$\rho = \rho_o \left(\frac{p + B}{p_o + B} \right)^{1/\gamma}, \text{ with } \gamma = 7,\ B = 1.67 \times 10^9. \tag{22}$$

In Equation (22), the reference density and pressure were set to $\rho_o = 534\,\mathrm{kg/m^3}$ (density of solid lithium) and $p_o = 10^5\,\mathrm{Pa}$. Another important simplifying assumption for approximating solid lithium was the use of an isotropic Newtonian viscous stress tensor with a high constant value of dynamic viscosity $\mu_{\mathrm{Li}} = 1000\,\mathrm{Pa \cdot s}$ (see Appendix A). For the experiments and parameter space considered here, using this simple model produced good results, as discussed later in this section. Magnetic diffusivity was set as a constant with a nominal value of $\eta_{\mathrm{Li}} = 0.1\,\mathrm{m^2/s}$, which corresponds to that of solid lithium at 100 °C. We note that in reality, the magnetic diffusivity (electric resistivity) of lithium depends on its local temperature and pressure, and such dependencies can be taken into account in the OpenFOAM model. However, for simplicity, we ignore these effects and analyze only the sensitivity of the results to different constant values of η_{Li}.

Snapshots (rz cross-section) of the lithium ring, along with contours of the poloidal flux per radian ψ are shown in Figure 10 for several time instances during the implosion. Poloidal flux contours are shown for the range of $-0.3\,\mathrm{Wb/rad} \leq \psi \leq 0$ with $\Delta\psi = 0.03\,\mathrm{Wb/rad}$, and this range is the same for all instances. The poloidal flux contours are coloured by the magnitude of the magnetic field in the range of $0 \leq |\mathbf{B}| \leq 8\,\mathrm{T}$. These results are obtained with the nominal set of parameters listed above.

One can see that at early times, a strong magnetic field is generated in the gap between the outer surface of the lithium ring and the electromagnetic coil assembly. This magnetic field is generated by the electric current flowing through the coils during the discharge of the capacitor bank. The Lorentz force resulting from the induced electric current at the outer surface of the lithium ring acts upon the ring in the radial direction, initiating the implosion. At later times, the strength of the magnetic field in the gap decreases due to three different effects which are interconnected: (i) the movement of the ring (change in inductance of the system), (ii) the diffusion of the magnetic field into the ring, and (iii) the decay of the electric current flowing through the coil. It can also be seen that the magnetic field curves around the top and bottom of the ring. As such, some magnetic field is also present inside the ring, and this too diffuses into the ring through the inner surface.

In Figure 11, radial profiles of the magnetic field at the equator (along the dashed line in Figure 10a) are plotted with solid red lines for the same instances as in Figure 10. For comparison, the profiles obtained without the lithium ring in the computational setup are plotted with the black dashed lines. The radial positions of the lithium ring and compression coil are shown by the grey and pink shaded regions, respectively. First, one can see that as expected, the magnetic field inside the coil is zero. It may further be noted that the presence of the ring has a minor effect on the profiles of the magnetic field outside the coil (to the right of the pink-shaded area). Looking at the evolution of the magnetic field profile inside the ring (region shaded grey), the following can be observed: (i) At early times, a strong magnetic field generated in the gap starts to diffuse into the ring. At the same time, because of the magnetic field bending around the ring, a weaker magnetic field of the opposite sign diffuses into the ring from the inside as well. (ii) Once the ring moves inward, the magnetic field in the gap quickly drops, mainly due to the change in inductance. As such, the magnetic field present in the gap at the outer surface of the ring becomes weaker than that diffused into the ring. As a result, the direction of the Lorentz force acting upon the ring in this region is reversed, consequently putting the material under tension. It should be noted that, in the case of liquid liners, this may result in delamination and the formation of a cavitated liquid region [34]. Since a highly deformable solid is modelled

here as a high-viscosity liquid, delamination and cavitation are observed in our simulations when the viscosity of the ring is set below a certain threshold.

In our experiments of the electromagnetic implosion of solid lithium rings, no bulk delamination was observed on the outer surface of the ring. Hence, the lower bound of the viscosity values used in this work was selected just above the threshold at which cavitation occurs. For the parameters of the current experiments, this value is approximately 200 Pa · s. Additional simulations were also performed in which viscosity was varied by an order of magnitude (in the range of 200 Pa·s $\leq \mu_{\text{ring}} \leq$ 2000 Pa·s). It is worth mentioning that this viscosity range is similar to that of other highly-viscous liquids, such as peanut butter or silicone sealant (100–1000 Pa·s). The effect of viscosity on the shape of the ring and the implosion trajectory was found to be insignificant (within the tested range), and all the results reported in this work were obtained using a nominal value of $\mu_{\text{ring}} = 1000$ Pa·s. Lastly, profiles of the magnetic field obtained in simulation without a ring (dashed black lines in Figure 11) exhibit very similar behaviour at all times, as expected. These profiles correspond to the magnetic field inside a solenoid of finite length with the field strength directly proportional to the electric current in the coil.

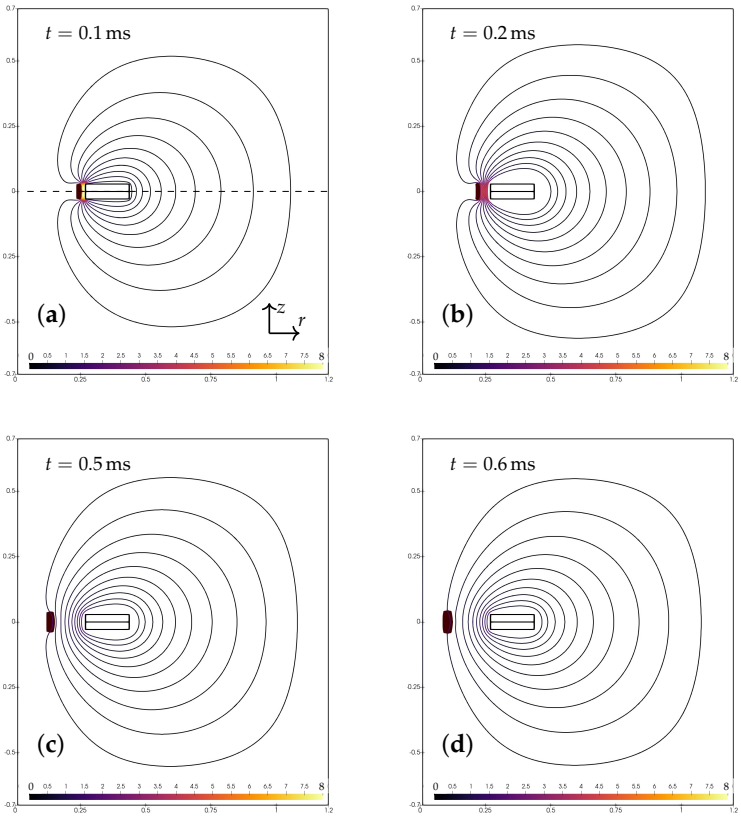


Figure 10. Snapshots of the lithium ring and magnetic field at several time instances during the implosion, as obtained in simulation with the nominal set of parameters ($\eta_{\text{ring}} = 0.1\,\text{m}^2/\text{s}$, $\eta_{\text{vac}} = 10^5\,\text{m}^2/\text{s}$). For all plots, contours of poloidal flux are shown for the same range of $-0.3\,\text{Wb/rad} \leq \psi \leq 0$, with $\Delta\psi = 0.03\,\text{Wb/rad}$. The contours are coloured by the magnitude of the poloidal magnetic field in the range of $0 \leq |\mathbf{B}| \leq 8\,\text{T}$.

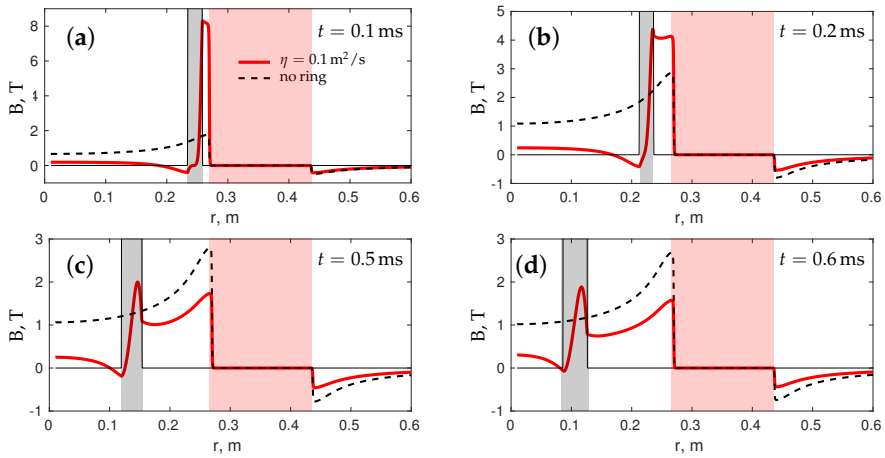


Figure 11. Radial profiles of the magnetic field at the equator $z = 0$. The solid red lines correspond to the lithium ring with $\eta_{\mathrm{ring}} = 0.1\,\mathrm{m}^2/\mathrm{s}$, $\rho_{\mathrm{ring}} = 534\,\mathrm{kg}/\mathrm{m}^3$, and $\mu_{\mathrm{ring}} = 1000\,\mathrm{Pa}\cdot\mathrm{s}$. Shown by the black dashed lines are the profiles obtained for the case without a lithium ring present in the computational setup.

To illustrate the evolution of the shape of the lithium ring during the implosion, the *rz* cross-sections of the ring, as seen at different times, are plotted in Figure 12. The deformation and axial elongation of the ring can be observed from the early stages of the implosion. As the ring moves inward, it becomes thicker due to geometric convergence, and also continues to extend axially. Fine details with regard to its shape depend on the material model, but the overall dynamics remain consistent. To compare the trajectory from the simulation with experimental data, the position of the ring was extracted at three locations on the surface of the ring, as marked by the red, orange, and blue dots in Figure 12.

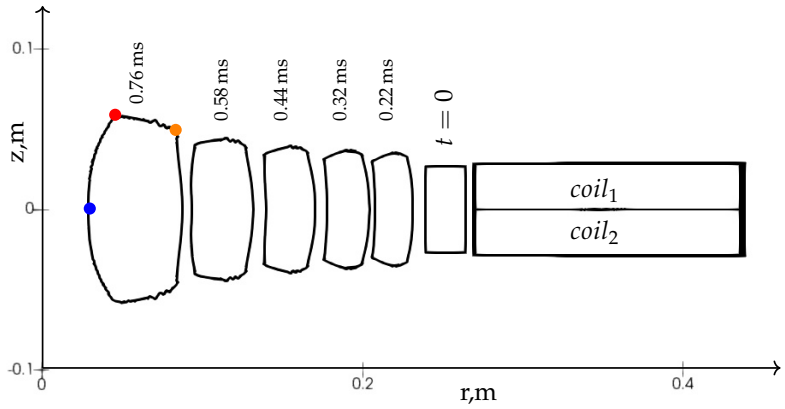


Figure 12. The shape and position of the lithium ring during the implosion (*rz* cross-section). Results are shown for the same set of parameters used in Figures 10 and 11. In simulation, trajectories were extracted for three parts of the ring as marked by the coloured dots. In the experiment, the trajectories of the inner and outer surfaces of the ring (red and orange dots) were obtained by analysis of the high-speed video, with partial data also available for the inner surface of the ring at the equator (blue dot).

3.1.3. Comparison with Experimental Data

We first validate our numerical model of the external circuit connected to the electromagnetic coil by evaluating how well it reproduces the experimental electric currents obtained in the compression coil assembly without a lithium ring. Results are shown in Figure 13. The experimental current for an initial capacitor voltage of $V_o = 14\,\mathrm{kV}$ is shown by the solid black line. The current obtained in the simulations is shown by the red lines. The solid red line corresponds to a case with $V_o = 14\,\mathrm{kV}$ as in the experiment, and the

dashed red line corresponds to the scaled voltage of $V_o = 14/1.167 = 12\,\text{kV}$, in which the initial voltage is scaled by the ratio of the peak currents obtained in the experiment and in simulation. The reason behind the difference in peak currents is unknown, but can probably be attributed to parasitic losses that are not accounted for in the model. The experiment was also carried out at a different voltage, and the scaling factor for the peak currents was found to be identical. As such, the experimental capacitor voltage was scaled by the same factor in all simulations of the imploding ring. With the scaled voltage, the experimental and simulated currents are in excellent agreement until about 0.25 ms (compare the solid black and dashed red lines). The discrepancy at later times is due to two reasons. The first is that when the real circuit is simplified to a set of effective circuit parameters for use in simulations, this is done by finding the best fit (the experimental circuit is too complex to be reduced to a theoretical RLC circuit analytically). Finding parameters that give a good fit at all times proved to be difficult, so achieving a good fit at earlier times was prioritised, as the initial current ramp has a dominant effect on the ring's trajectory. The second is that the time at which the diode turns on in the simulation and in the experiment is likely to be slightly different because the diode in the experimental circuit is not ideal. Therefore, the decay of the current at later times may be a bit different. It is worth pointing out that the trajectory of the ring is primarily determined by what happens at the very beginning, because once the implosion commences, the magnetic push rapidly diminishes and the ring mainly coasts due to its inertia.

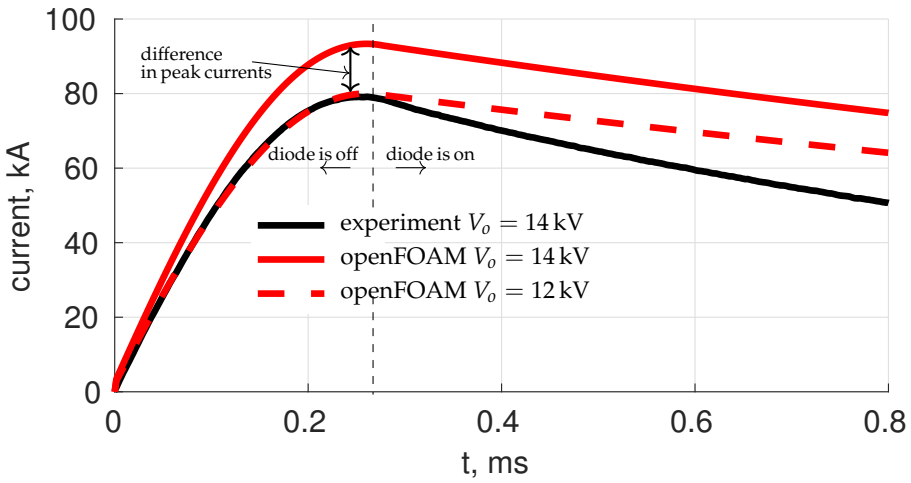


Figure 13. Electric current in the coil obtained in the experiment with no lithium ring present. This experiment was used to calibrate the capacitor bank voltage used in the simulations. The experimentally measured current and the current obtained from the simulation for $V_o = 14\,\text{kV}$ are shown by the solid black and solid red lines, respectively. The additional simulation for the voltage $V_o = 12\,\text{kV}$ (original voltage $V_o = 14\,\text{kV}$ scaled by the ratio of the peak currents in the experiment and the simulation, $I_{max_{sim}} / I_{max_{exp}} = 1.167$) is shown by the dashed red line. Based on these results, the voltage of the capacitor was reduced by a factor of 1.167 in all simulations.

The comparison between the electric current obtained in the experiment and the simulations for the case of an imploding lithium ring is shown in Figure 14. Experimental results are shown as solid and dashed black lines, corresponding to the currents in the top and bottom coils, respectively. As expected, the experimental currents in both coils are nearly identical. Simulation results are shown by several red and magenta lines, which correspond to different resistivity values of the ring, with all other parameters kept unchanged ($\rho_{\text{ring}} = 534\,\text{kg/m}^3$, $\mu_{\text{ring}} = 1000\,\text{Pa}\cdot\text{s}$, $\eta_{\text{vac}} = 10^5\,\text{m}^2/\text{s}$, $V_o = 12\,\text{kV}$). The red dotted, solid, and dashed lines correspond to ring magnetic diffusivities of

$\eta_{\text{ring}} = 0.05$, 0.1, and $0.2\,\text{m}^2/\text{s}$, respectively. The current obtained for $\eta_{\text{ring}} = 0.5\,\text{m}^2/\text{s}$ is shown by the magenta line.

First, one can see that the shape of the current curve in the experiment of the imploding ring is different from that obtained without the ring in the setup (compare Figures 13 and 14). This difference stems from the fact that the presence of the ring alters the inductance of the system. Moreover, the inductance of the system continues to change as the ring moves inward. Thus, the electric current in the coil depends on the implosion trajectory, as well as the applied voltage and circuit parameters. Second, varying the magnetic diffusivity of the ring in the range $0.05\,\text{m}^2/\text{s} \le \eta_{\text{ring}} \le 0.5\,\text{m}^2/\text{s}$ results in a noticeable change in the current, with simulation results approaching experimental data for higher values of magnetic diffusivity. For a magnetic diffusivity of $\eta_{\text{ring}} = 0.5\,\text{m}^2/\text{s}$, the numerical and experimental results are in very good agreement (compare the magenta and black lines).

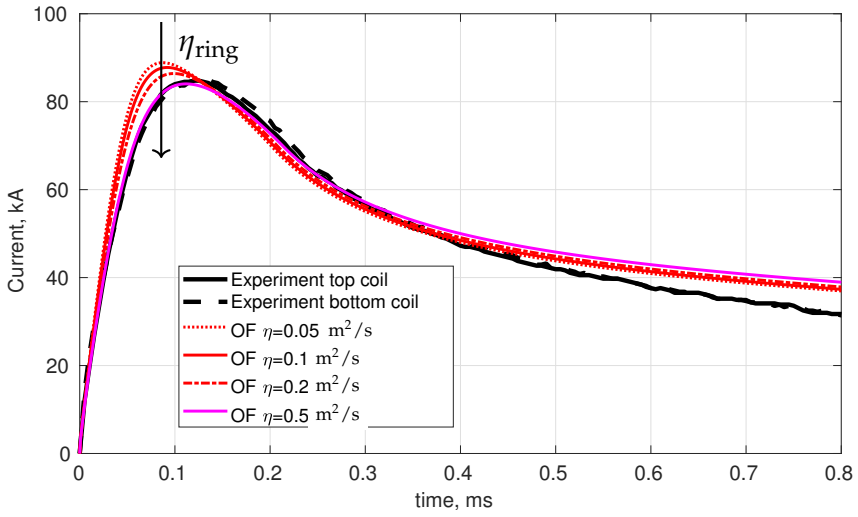


Figure 14. Comparison between the electric current in the coil measured in the experiment and calculated in the simulations. Experimental data for the top and bottom coils are shown by the black solid and dashed lines, respectively. Simulations were carried out for several values of magnetic diffusivity of the lithium ring in the range of $0.05\,\text{m}^2/\text{s} \le \eta_{\text{ring}} \le 0.5\,\text{m}^2/\text{s}$, with all other parameters kept unchanged. The solid red line corresponds to $\eta_{\text{ring}} = 0.1\,\text{m}^2/\text{s}$, which is the nominal magnetic diffusivity for solid lithium at a temperature of 100 °C (temperature at which the experiment was performed). The red dash-dot line corresponds to $\eta_{\text{ring}} = 0.2\,\text{m}^2/\text{s}$, which is the nominal magnetic diffusivity of liquid lithium just above the melting temperature. The solid magenta line corresponds to $\eta_{\text{ring}} = 0.5\,\text{m}^2/\text{s}$ (capacitor voltage is $V_o = 12\,\text{kV}$ in simulations and $V_o = 14\,\text{kV}$ in the experiment, $\rho_{\text{ring}} = 534\,\text{kg}/\text{m}^3$, $\mu_{\text{ring}} = 1000\,\text{Pa}\cdot\text{s}$, $\eta_{\text{vac}} = 10^5\,\text{m}^2/\text{s}$).

The comparison between the experimental and numerical trajectories of the lithium ring is shown in Figure 15 for the same set of simulations as those shown in Figure 14. Parts (a) and (b) of the figure correspond to the trajectories of the inner and outer surfaces of the lithium ring at the locations marked by the orange and red dots in Figure 12, respectively. The experimental trajectory is shown by the black line. The trajectories obtained in simulations for different values of magnetic diffusivity of the ring are shown by the red lines and marked with different symbols as specified in the legend. Part (c) of the figure shows the relative deviations of the simulated trajectories from the experimental ones. It is evident that the magnetic diffusivity of the ring significantly influences its trajectory. At early times, all trajectories align well with the experimental data for both the inner and outer surfaces of the ring, whereas at later times the implosion proceeds faster for lower values of magnetic diffusivity. This is because the lower the magnetic

diffusivity, the less the magnetic field diffuses into the ring, resulting in a stronger initial push. It is also worth noting that, after the initial acceleration phase, the position of the ring changes nearly linearly with time for all simulations. The ring accelerates rapidly due to the electromagnetic push, and then continues to coast inward at an approximately constant velocity for the remainder of the implosion. This velocity is determined by the short period of time when the current in the coil is ramping up and the ring has only just begun to move from its initial position. When comparing numerical and experimental trajectories, it can be seen that the trajectories are in better agreement for higher values of magnetic diffusivity, in particular, for $\eta_{\text{ring}} = 0.2\ \text{m}^2/\text{s}$ and $\eta_{\text{ring}} = 0.5\ \text{m}^2/\text{s}$, the relative deviation is $\lesssim$20%. This aligns with the results for the electric current in the coil (see Figure 14).

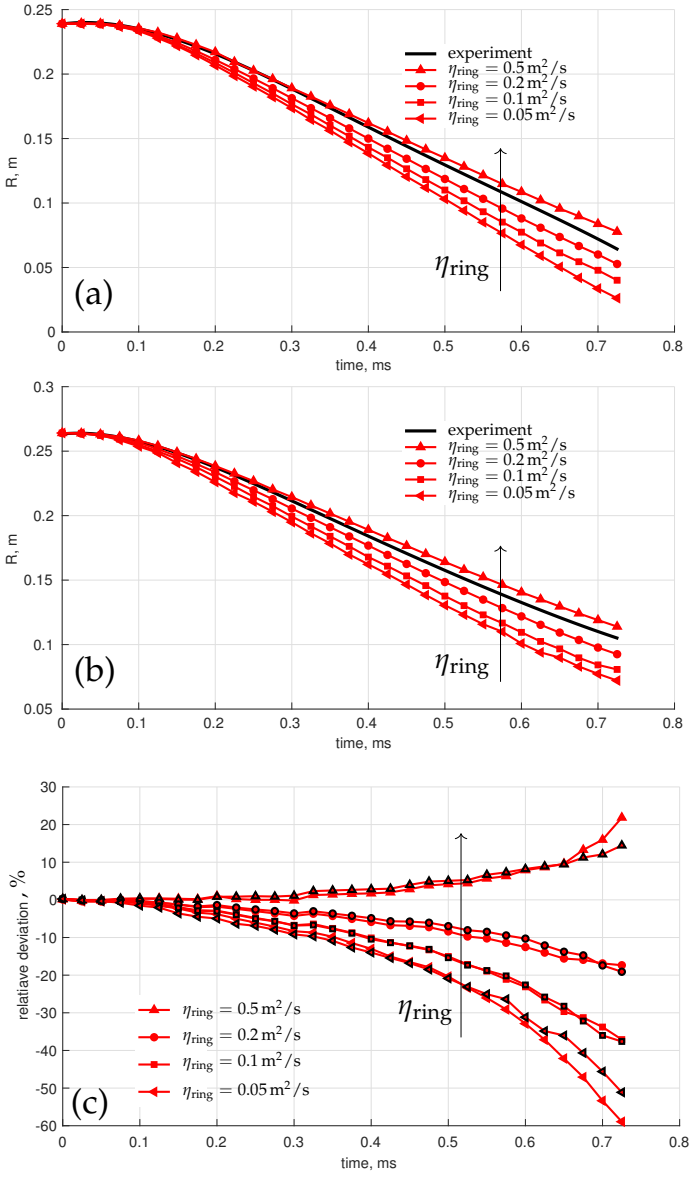


Figure 15. Effect of the magnetic diffusivity of the lithium ring on the implosion trajectory. (**a**) Inner surface at the location marked by the red dot in Figure 12; (**b**) outer surface at the location marked by the orange dot in Figure 12; (**c**) relative deviation $((R_{\text{sim}} - R_{\text{exp}})/R_{\text{exp}})$ of simulated trajectories from experimental ones for both surfaces; results for the outer surface are shown with black markers. Experimental trajectories in (**a**,**b**) are shown by the solid black lines. OpenFOAM results are shown by the solid red lines with the corresponding markers: ◀—$\eta_{\text{ring}} = 0.05\,\text{m}^2/\text{s}$; ■—$\eta_{\text{ring}} = 0.1\,\text{m}^2/\text{s}$; ●—$\eta_{\text{ring}} = 0.2\,\text{m}^2/\text{s}$; ▲—$\eta_{\text{ring}} = 0.5\,\text{m}^2/\text{s}$. Capacitor voltage is $V_o = 12\,\text{kV}$ in simulations and $V_o = 14\,\text{kV}$ in the experiment, $\rho_{\text{ring}} = 534\,\text{kg}/\text{m}^3$, $\mu_{\text{ring}} = 1000\,\text{Pa}\cdot\text{s}$, and $\eta_{\text{vac}} = 10^5\,\text{m}^2/\text{s}$.

Figure 16 shows the trajectories of the inner surface measured at the top and at the equator of the ring (marked by the orange and blue dots in Figure 12). Experimental trajectories are plotted with the black lines, and the solid and dashed lines correspond to the top and the equator, respectively. The trajectories obtained from the simulations are shown with magenta and red lines, corresponding to magnetic diffusivity values $\eta_{\text{ring}} = 0.05\,\text{m}^2/\text{s}$ and $\eta_{\text{ring}} = 0.5\,\text{m}^2/\text{s}$, respectively. As mentioned earlier, the experimental trajectory of the equator can only be measured once the equator bulges forward, as shown in Figure 12 at $t = 0.76\,\text{ms}$, since until then, it is not visible to the high-speed camera. In the experiment, the equatorial bulge appears at some time between $0.3\,\text{ms} < t < 0.4\,\text{ms}$, as indicated by the appearance of the dashed line. From the simulation results, one can see that the time at which the equatorial bulge appears depends on the magnetic diffusivity of the ring; an increase in magnetic diffusivity leads to an earlier formation of the equatorial bulge (as the dashed lines deviate from the solid lines). Simulations at other values of magnetic diffusivity also support the above. By comparing experimental and numerical data, it can be seen that, as in the previous plots, results for the higher value of magnetic diffusivity are in better agreement with the experiment.

Based on these simulation results, the magnetic diffusivity of the lithium ring in the experiment may be higher than expected from the nominal magnetic diffusivity of solid lithium at 100 °C, which is $\eta_{\text{ring}} = 0.1\,\text{m}^2/\text{s}$. One possible reason for this is the temperature dependence of lithium's magnetic diffusivity [35], which is not taken into account in our simplified model. However, the increase in lithium temperature due to ohmic heating is estimated to be approximately 10°–20 °C (so the lithium temperature is still well below the melting point $T_{melt} = 180.5$ °C under normal conditions), and this should have little effect on its magnetic diffusivity. Another factor which may affect the magnetic diffusivity is a phase transition of lithium, such as a change in the solid state structure or melting due to high pressures [36,37]. However, in our experiment, the pressures are below those which cause these phase transitions (the maximum magnetic pressure in the experiment is about 25 MPa). The most plausible explanation for the higher magnetic diffusivity of the ring in the experiment is the presence of a corrosion layer on the outer surface of the ring. Even if the corrosion layer is thin, it may affect the diffusion of the magnetic field into the ring at early times, which in turn would affect the trajectory and the current profile.

This experiment was also simulated with the commercial multiphysics code ANSYS LS-Dyna using a Johnson–Cook material model [38] for the lithium with some of the results reported in [32]. The Johnson–Cook model captures stress dependence on strain hardening, strain-rate hardening, and thermal softening and was calibrated using experimental data [39]. The trajectory and shape of the ring obtained in LS-Dyna and OpenFOAM are found to be in good agreement. Therefore, for the scope of this work, the use of a simple model of constant high viscosity is adequate, and studying the effect of the material model is left for future work.

To conclude, the numerical results obtained with our extended solver, where solid lithium is modelled as a highly viscous fluid with constant magnetic diffusivity, overall compare well with experimental data for the electromagnetic implosion of a solid lithium ring. Numerical simulations can be used to study the effects of various parameters, and magnetic diffusivity in particular was shown to be an important parameter to accurately predict implosion trajectories and the shape of the ring during the implosion.

3.2. Compressing Toroidal Flux by the Electromagnetic Implosion of a Hollow Lithium Cylinder onto a Centre Shaft

The primary focus of this section is on predictive modelling of the compression of toroidal magnetic flux confined between an imploding lithium liner and a centre shaft, in particular after the liner impacts the centre shaft.

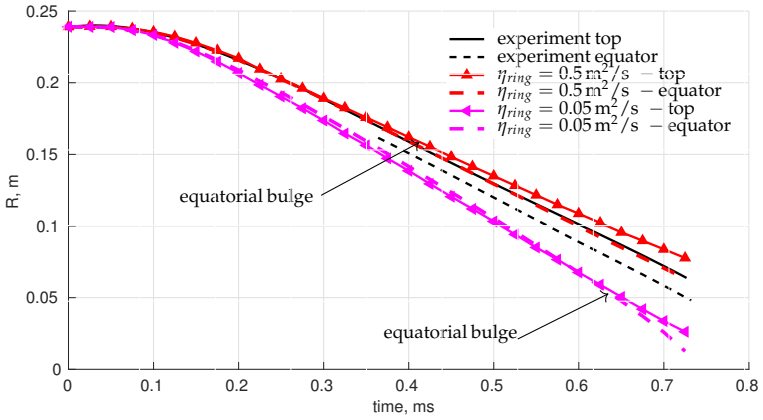


Figure 16. Effect of magnetic diffusivity on the evolution of the lithium ring's shape during the implosion (with all other parameters kept unchanged). Experimental data for the inner surface at the top and equator are shown by the black solid and dashed lines, respectively. Data from OpenFOAM simulations with two magnetic diffusivity values, $\eta_{\text{ring}} = 0.05\,\text{m}^2/\text{s}$ and $\eta_{\text{ring}} = 0.5\,\text{m}^2/\text{s}$, are shown by the red and magenta lines, respectively. The solid and dashed lines correspond to the top and equator of the inner surface (marked by the red and blue dots in Figure 12), respectively.

3.2.1. Experimental Setup

Figure 17 shows a schematic of the experimental apparatus, known as Prototype 0, used for the implosion of a cylindrical lithium liner onto an hourglass-shaped central structure (centre shaft). The apparatus consists of three main components: (i) a compression coil assembly connected to a high-voltage power supply, (ii) a solid, hollow, cylindrical lithium liner, and (iii) a replaceable centre shaft that houses diagnostics and also, after the liner lands on it, defines the shape of the vacuum cavity. Two variations of the centre shaft are shown in Figure 17b,c. The main difference between these designs is the angle at which the liner impacts the centre shaft. For the configuration shown in (b), the liner impacts the centre shaft at a slant (lands on the conical surface), whereas in (c), the impact is on the vertical cylindrical section (which lies beyond the edge of the conical surface). These types of impacts are referred to as "oblique" and "flat" landings, respectively. Prototype 0 is a scaled-down model of LM26, designed to test the electromagnetic compression system and collapse a vacuum cavity without the inclusion of magnetized plasmas.

To achieve stable compression of a magnetized plasma, the safety factor (q) must be maintained within a certain range [40,41]. The necessary condition for that is to increase the toroidal field during compression. In Prototype 0, the toroidal magnetic field is generated by running electric current through the centre shaft, referred to as the "shaft current" (I_{shaft}) later in this section. This is accomplished by connecting the centre shaft to a dedicated high-voltage capacitor bank. Prior to the liner making electrical contact with the centre shaft, the toroidal magnetic field is generated by discharging the capacitor bank through the external circuit. Once the liner and the centre shaft establish electrical contact, poloidal current starts to flow through the liner, forming a closed loop that encircles the vacuum cavity bounded by the centre shaft and the liner. When this happens, the toroidal flux inside the cavity becomes trapped. As the liner continues its inward motion, the volume of the vacuum cavity decreases and the trapped toroidal flux is compressed. In the ideal case where both the centre shaft and the liner are perfect conductors, the amplification of the toroidal field is inversely proportional to the inductance of the vacuum cavity. In practice, flux diffusion into the liner and centre shaft reduces the amplification. The amount of diffused flux depends on the materials of the centre shaft and the liner, as well as on the implosion speed. The main goal of modelling this experiment with OpenFOAM is to compare numerical predictions of toroidal magnetic field amplification with experimental data and to explore the sensitivity of the results to various parameters.

The compression coil assembly shown in Figure 17 is an extended version of the one used to implode a lithium ring, as described in Section 3.1. In Prototype 0, the compression coil assembly consists of 48 single-turn aluminum plates, each 6.4 mm thick. The nominal inner and outer radii of each plate are $R_{\text{coil}_{\text{inner}}} = 0.234\,\text{m}$ and $R_{\text{coil}_{\text{outer}}} = 0.411\,\text{m}$, respectively. The height of the compression coil assembly is $H_{\text{coil}} = 0.367\,\text{m}$. Adjacent aluminum plates are separated by a thin layer of laminated insulation. Sets of three sequential aluminum plates are connected in series to form individual coils, yielding a stack of 16 coils in total, each comprising three turns. In the experimental apparatus, there are eight independent RLC circuits, each connected to a pair of coils located symmetrically about the equator. Each circuit is powered by twenty-four high-voltage 52 μF capacitors which can be charged up to 16 kV. Depending on the purpose of the experiment, some coil pairs may be disconnected and treated as "open-circuited". For additional details about the experimental apparatus, liner production, and available diagnostics, see [42].

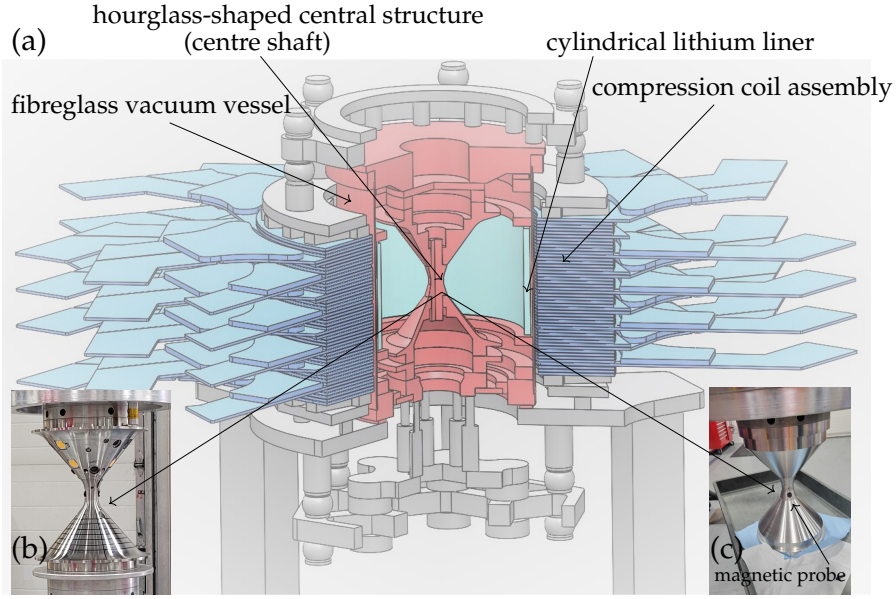


Figure 17. Schematic of the Prototype 0 experimental apparatus for the implosion of a cylindrical lithium liner onto an hourglass-shaped central structure (part (**a**)). The centre shaft is replaceable and can be reconfigured between experiments. Two examples of the centre shaft are shown: (**b**) for oblique and (**c**) for flat liner landings.

3.2.2. Numerical Setup

For a solid lithium cylinder imploded onto an hourglass-shaped central structure, predictive modelling is more challenging because of the interaction between the liner and the solid multi-material structure, as well as the diffusion of the magnetic field into that structure. The rigid multi-material structure is represented by sets of dedicated grid cells with the magnetic diffusivity of a specific material assigned to each set. The computational mesh is fitted to the geometry of the rigid structure, so each grid cell is strictly inside or outside the structure. For grid cells representing rigid structure, the momentum equation is not solved to enforce zero velocity. With this approach, in the solid regions, only magnetic diffusion is solved. In addition, the evolution of the toroidal field generated by the current flowing through the centre shaft also needs to be modelled.

The cross-section of the computational setup is shown in Figure 18. The entire computational domain and a zoomed view of the centre shaft, the liner, and the compression coil assembly are shown in parts (a) and (b) of the figure, respectively. Conceptually, the numerical setup is similar to that used in simulations of the electromagnetic implosion of a lithium

ring (see Section 3.1). The centre shaft is composed of three materials, marked by different colours and denoted as "sol_1", "sol_2", and "sol_3" in Figure 18b. In Figure 18, the solid part "sol_1" (blue) corresponds to the "oblique" landing configuration, while modifications to this part for a "flat" landing are shown by the black lines (parts denoted as "removable"). The initial position of the lithium cylinder is shown in dark red. The compression coil assembly is modelled as a stack of 16 separate coils, each with three turns, and a 1 mm vacuum gap between each pair of adjacent coils. For simplicity, in the simulation setup, each of the 16 coils is connected to its own RLC circuit, unlike in the experimental setup, where 2 coils (symmetrically located about the equator) are connected to a single high-voltage capacitor bank. A subset of coils was deactivated (i.e., "open circuited") as shown in Figure 18, where active coils are marked with ✓ and deactivated with ✗. In the simulations, deactivated coils were modelled by enforcing zero toroidal current through them.

The extent of the computational domain in the radial and axial directions is $0.01 \leq r[\mathrm{m}] \leq 1.2$ and $-0.6 \leq z[\mathrm{m}] \leq 0.6$, respectively. The background mesh has $\Delta r = \Delta z = 2\,\mathrm{mm}$ resolution, with three levels of refinement such that the resolution in the area of interest is $\Delta r = \Delta z = 0.25\,\mathrm{mm}$. The nominal inner and outer radii of each coil, as well as the axial extent of the compression coil assembly, are identical to those in the experimental apparatus. The height of each individual coil is $h_{\mathrm{coil}} = 0.022\,\mathrm{m}$.

For all the results presented in this section, the initial dimensions of the lithium cylinder are as follows: inner radius $R_{\mathrm{cylinder_{inner}}} = 0.206\,\mathrm{m}$, outer radius $R_{\mathrm{cylinder_{outer}}} = 0.2175\,\mathrm{m}$, and height $H_{\mathrm{cylinder}} = 0.257\,\mathrm{m}$. The initial gap between the inner radius of the coil and the outer radius of the lithium cylinder is 16.5 mm. Effective circuit parameters are identical for all coils and are set as follows: $R_{\mathrm{cap}} = 0.0165\,\Omega$, $L_{\mathrm{cap}} = 166.67\,\mathrm{nH}$, $C_{\mathrm{cap}} = 624\,\mu\mathrm{F}$, $R_{\mathrm{cable}} = 0.0085\,\Omega$, $L_{\mathrm{cable}} = 300\,\mathrm{nH}$, and $V_o = 11500\,\mathrm{V}$. The nominal magnetic diffusivity, density, and viscosity of the lithium cylinder are $\eta_{\mathrm{cylinder}} = 0.1\,\mathrm{m^2/s}$, $\rho_{\mathrm{cylinder}} = 534\,\mathrm{kg/m^3}$, and $\mu_{\mathrm{cylinder}} = 1000\,\mathrm{Pa{\cdot}s}$. The magnetic diffusivity for vacuum is set to $\eta_{\mathrm{vac}} = 10^5\,\mathrm{m^2/s}$ and the maximum time step is $\mathrm{dt_{max}} = 10^{-8}\,\mathrm{s}$. Nominal magnetic properties of the rigid solid materials are set as follows: "sol_1"—aluminum with $\eta_{\mathrm{sol_1}} = 0.02\,\mathrm{m^2/s}$, "$sol_2$"—stainless steel with $\eta_{\mathrm{sol_2}} = 0.55\,\mathrm{m^2/s}$, and "$sol_3$"—ideal conductor $\eta_{\mathrm{sol_3}} = 0$.

The initial and boundary conditions are identical to those for the implosion of the lithium ring for all variables, except for the toroidal field function F. For a known value of centre shaft current I_{shaft}, the value of the toroidal field function in the vacuum can be calculated as:

$$F_{\mathrm{vac}} = \frac{\mu_o}{2\pi} \cdot I_{\mathrm{shaft}}. \tag{23}$$

Equation (23) is used to prescribe values of the toroidal function F in the vacuum region of the computational domain. One way to do this is to assume that the toroidal magnetic field corresponding to the specific value of $I_{\mathrm{shaft}} = I_o$ is generated instantaneously, after which the external circuit is disconnected. In this scenario, the value $F = F_o$ is imposed in the vacuum region of the computational domain as the initial condition, and then the toroidal function F evolves according to Equation (3). The boundaries of the computational domain are treated as perfect conductors ($\partial F/\partial n = 0$), thereby the total toroidal flux in the domain is conserved during the simulations. An alternative method to impose a toroidal field is to use experimental data for the shaft current $I_{\mathrm{shaft}}(t)$ to overwrite the value of the toroidal function in the vacuum at each time step (via Equation (23)), up to the point when the liner and centre shaft make electrical contact. Beyond this point, F evolves in accordance with Equation (3). Both methods were tested, and the amplification of the toroidal field was confirmed to be identical; therefore, the first (simpler) approach was used in the simulations.

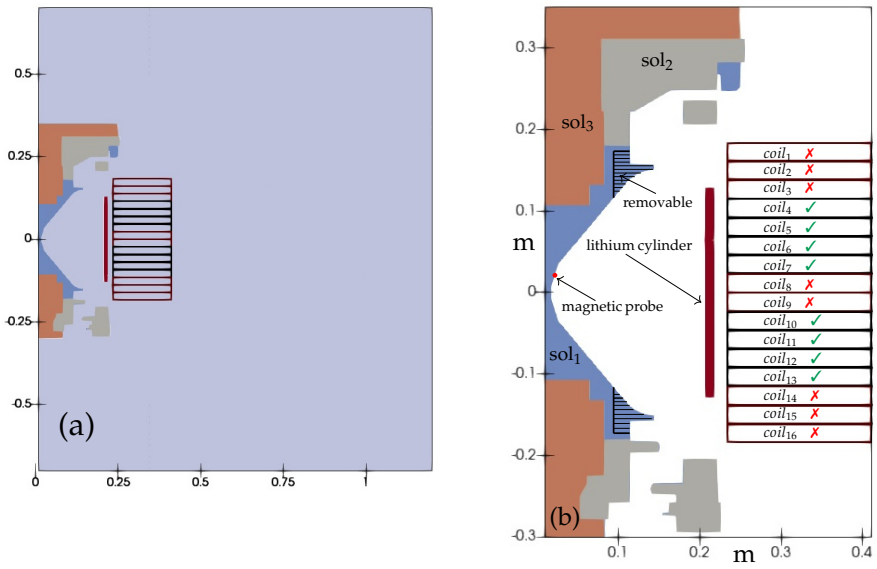


Figure 18. Simulation setup for the imploding cylinder simulations. (**a**) Full computational domain; (**b**) detailed view of the centre shaft and compression coil assembly. Green tick marks and red crosses indicate which coils are in use and which are deactivated, respectively. The initially cylindrical liner is depicted in dark red. The magnetic probe, used to measure both the poloidal and toroidal components of the magnetic field, is located at the position marked by the red dot.

3.2.3. Liner Trajectory

Figure 19 demonstrates the code's ability to simulate the electromagnetic implosion of a solid lithium cylinder onto a rigid structure, highlighting the sensitivity of the results to minor changes in the geometry of the electromagnetic coils and configuration of the centre shaft ("oblique" or "flat" landing). In simulations, we explore the effect of increasing the inner radius of the deactivated coils, ΔR_{inner}, specifically for coils 1, 2, 3, 8, 9, 14, 15, and 16 as shown in Figure 18b. The shape and trajectory of the liner are shown for the five simulations. The first row in Figure 19 corresponds to a "flat" landing with $\Delta R_{\text{inner}} = 0$; the second row shows an "oblique" landing with $\Delta R_{\text{inner}} = 0$; the third, fourth, and fifth rows show "oblique" landings with $\Delta R_{\text{inner}} = 1\,\text{mm}$, 3 mm, and 6 mm, respectively. All other parameters remain unchanged between the simulations. The poloidal magnetic field generated by the compression coil is shown by the contours of the poloidal flux function ψ, using the same range of values in all plots.

Before delving into the details, one can observe several common features across all cases: (i) the top and bottom of the lithium cylinder are deformed by the poloidal magnetic field generated by the compression coils, as the field lines bend around the liner; (ii) when the lithium liner comes in contact with the centre shaft, an enclosed vacuum cavity is formed; (iii) the lithium liner slides along the centre shaft collapsing the vacuum cavity; (iv) the poloidal field diffuses into both the liner and centre shaft; and (v) a portion of the poloidal field may penetrate through the liner and subsequently be compressed by it in the late stages of the implosion.

Comparing simulation results for the "flat" and "oblique" landings (first and second rows of the figure), one can see that by modifying the geometry of the centre shaft, we can tune the impact and initial interaction between the liner and the structure (compare regions inside yellow circles) without significantly altering the shape of the vacuum cavity. For a "flat" landing, the contact between the lithium liner and the centre shaft occurs over a larger surface area, which may influence how the toroidal flux is trapped. One can also see that in the late stages of the implosion, near the back surface at the top and bottom

of the liner, the colour changes from dark red to pink; see snapshots at $t = 0.7$ ms in the first and second rows. This indicates that those regions are under tension, which could be because of pressure waves resulting from the impact between the liner and centre shaft, or stretching of the liner by magnetic field lines diffused into it.

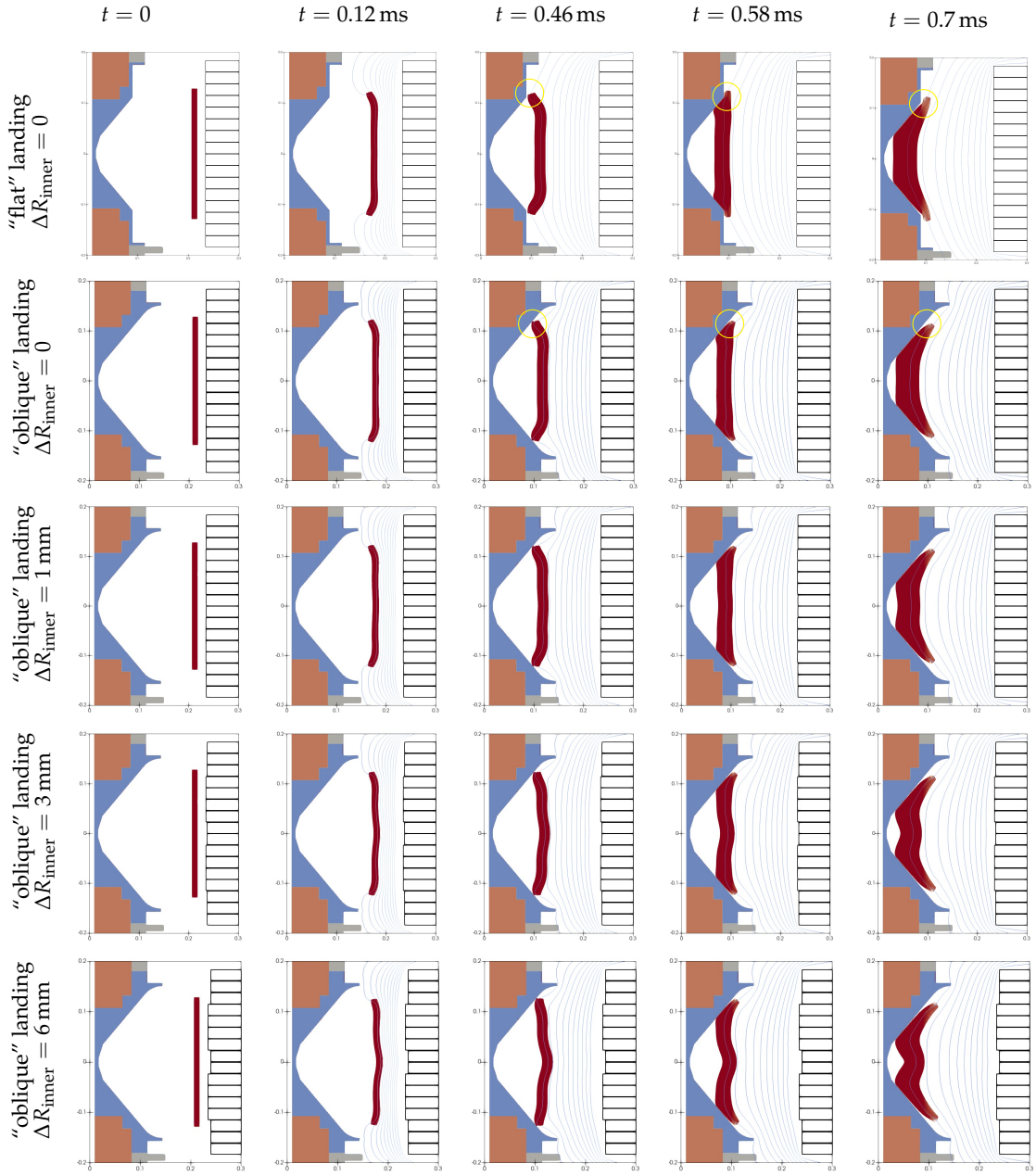


Figure 19. Effect of the centre shaft configuration and variation in the inner radius of deactivated coils on the shape of the liner and its implosion trajectory. Rows 1–5 correspond to "flat" landing with $\Delta R_{\text{inner}} = 0$ (nominal), and "oblique" landings with $\Delta R_{\text{inner}} = 0$ (nominal), 1 mm, 3 mm, and 6 mm. The contours of the poloidal flux ψ in all plots are shown over an identical range of values: $-0.02\,\text{Wb/rad} \leq \psi \leq -0.002\,\text{Wb/rad}$: 10 contours with $\Delta\psi = 0.002\,\text{Wb/rad}$. $\eta_{\text{cylinder}} = 0.1\,\text{m}^2/\text{s}$, $\eta_{\text{sol}_1} = 0.02\,\text{m}^2/\text{s}$, $\eta_{\text{sol}_2} = 0.55\,\text{m}^2/\text{s}$, $\eta_{\text{sol}_3} = 0$, $V_o = 11500\,\text{V}$, and coils 1, 2, 3, 8, 9, 14, 15, and 16 are deactivated (zero toroidal current is enforced in those coils).

The effect of a small increase in the inner radius of the deactivated coils on the shape of the lithium liner during implosion is demonstrated in rows 3–5 of Figure 19. These results illustrate that small geometric modifications to subsets of the coils can alter the liner shape, highlighting the flexibility of the design offered by a multi-coil compression assembly. The

rationale for exploring the effect of increasing the inner radius of the deactivated coils lies in the fact that magnetic diffusion into those coils is not accounted for in the current implementation. The impact of neglecting magnetic diffusion is generally minor when all coils are active; however, it can become more significant when some coils are deactivated. When the shapes of the liners are visually compared to those in the experiments, increasing the inner radius of deactivated coils in the range of $2\,\text{mm} \leq \Delta R_{\text{inner}} \leq 4\,\text{mm}$ appears to lead to better agreement. In the experiments, the lithium liner exhibits some degree of buckling, so comparing the exact shape is not really possible. Lastly, it is also worth noting that the time at which the liner comes in contact with the centre shaft is approximately the same in all cases. The ANSYS LS-DYNA commercial software (version R16) was also used to simulate the liner trajectory in this experiment, with results reported in [42]. Overall, the shapes and trajectories of the liner obtained with different codes are in good agreement; therefore, they are only briefly summarized in this work, while the focus is placed on magnetic flux compression.

The time evolution of the poloidal field is shown in Figure 20. Experimental results are given for the magnetic probe located at $r_{\text{probe}_{\text{exp}}} = 16.4\,\text{mm}$, $z_{\text{probe}_{\text{exp}}} = 20\,\text{mm}$ (which is inside the centre shaft as shown in Figure 17c), and simulation results are shown for the first grid cell outside the centre shaft for $z = 20\,\text{mm}$, corresponding to $r = 21.7\,\text{mm}$ (marked by the red dot in Figure 18b). Simulation results are shown for "flat" and "oblique" landings for the $\Delta R_{\text{inner}} = 0$ and $\Delta R_{\text{inner}} = 3\,\text{mm}$ cases. Dimensional data obtained in the simulations are plotted in part (a) of the figure, and the same data normalized by the value at $t = 0.4\,\text{ms}$ are plotted in part (b), together with normalized experimental data shown by the red line. One can see that, for the cases considered, modification of the geometry of the centre shaft has very little effect on the evolution of the poloidal field. However, increasing the inner radius of the deactivated coils does affect the poloidal field evolution, and for the nominal geometry ($\Delta R_{\text{inner}} = 0$), the poloidal field increases faster. One can also see that there is good agreement between the numerical and experimental results, and that alignment is better for simulations with the increased inner radius of the deactivated coils. This supports observations that the shape of the liner in simulations better matches that in the experiment when the inner radius of the deactivated coils is slightly increased.

3.2.4. Toroidal Flux Compression

Compression of the toroidal flux enclosed by the centre shaft and the liner was observed in the Prototype 0 experiment, and here we examine to what extent it can be reproduced in simulations. The experimental measurements are shown in Figure 21. For plasma stability in LM26, the goal is to time the shaft current ramp with the implosion of the liner. However, in Prototype 0 tests, it was activated earlier and shaft current was already decaying when the implosion commenced. The shaft current generated by the external circuit is plotted by the dashed line. The electric current measured by the toroidal magnetic probe ($r_{\text{probe}_{\text{exp}}} = 17.5\,\text{mm}$, $z_{\text{probe}_{\text{exp}}} = 20\,\text{mm}$, Figure 18c, $I_{\text{shaft}} = 2\pi r_{\text{probe}} B_\phi / \mu_o$) is shown by the solid line. In this experiment, the compression coil was activated at $t = 0$ and the lithium liner impacted the centre shaft at about $t = 0.49\,\text{ms}$. One can see that until the lithium liner impacts the centre shaft, the electric current measured by the toroidal magnetic probe follows the one provided by the external circuit closely. Shortly after impact, the curves begin to deviate from each other; the electric current measured by the toroidal magnetic probe increases, whereas the current supplied by the external circuit continues to decay. The increase in current measured by the magnetic probe indicates that the liner and the centre shaft are in electrical contact and that the enclosed toroidal flux is being compressed, resulting in amplification of the toroidal field inside the vacuum cavity.

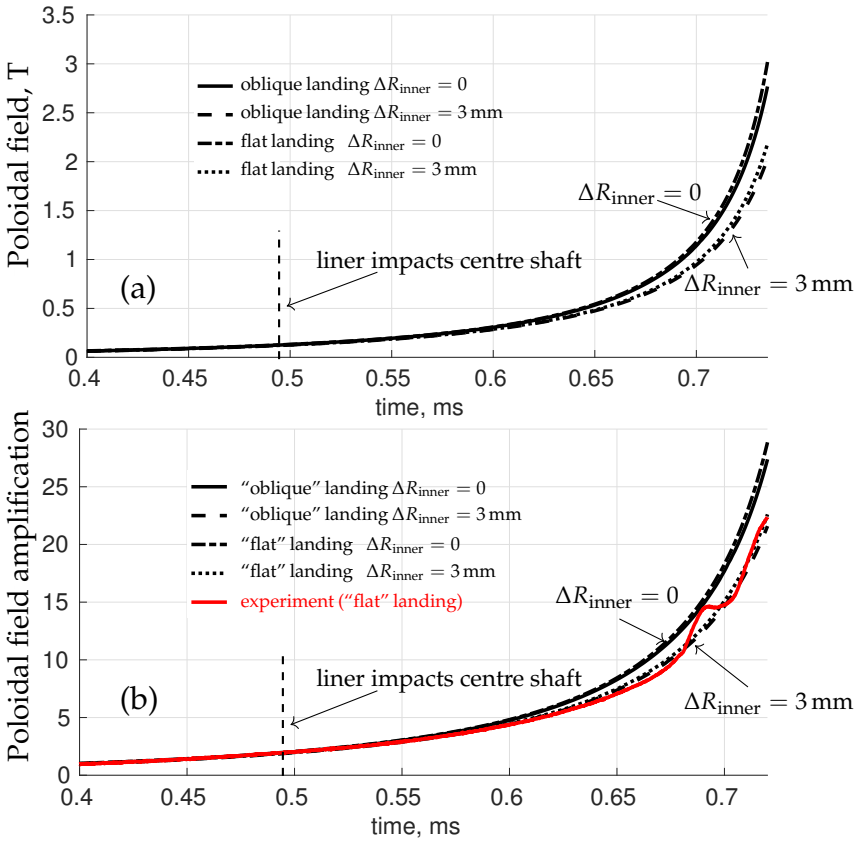


Figure 20. Evolution of the poloidal field; experimental data from a magnetic probe ($r_{\text{probe}_{\text{exp}}} = 16.4$ mm, $z_{\text{probe}_{\text{exp}}} = 20$ mm, shown in Figure 17c). Simulation results are shown by the black lines for the four cases: solid line—"oblique" landing, $\Delta R_{\text{inner}} = 0$ (nominal case); dashed line—"oblique" landing, $\Delta R_{\text{inner}} = 3$ mm; dash-dot line—"flat" landing, $\Delta R_{\text{inner}} = 0$; and dotted line—"flat" landing, $\Delta R_{\text{inner}} = 3$ mm. In the simulations, the data are extracted in the first grid cell outside the centre shaft for $z = 20$ mm ($r = 21.7$ mm). (**a**) Dimensional poloidal field obtained in simulations; (**b**) the same simulation data as in (**a**) but normalized by its value at $t = 0.4$ ms together with experimental data which are also normalized at $t = 0.4$ ms to compare with the simulation. Magnetic diffusivity is $\eta_{\text{cylinder}} = 0.1\,\text{m}^2/\text{s}$, $\rho_{\text{cylinder}} = 534\,\text{kg}/\text{m}^3$, $\mu_{\text{cylinder}} = 1000\,\text{Pa}\cdot\text{s}$, $\eta_{\text{sol}_1} = 0.02\,\text{m}^2/\text{s}$, $\eta_{\text{sol}_2} = 0.55\,\text{m}^2/\text{s}$, $\eta_{\text{sol}_3} = 0$, $V_o = 11500$ V, and coils 1, 2, 3, 8, 9, 14, 15, and 16 are deactivated.

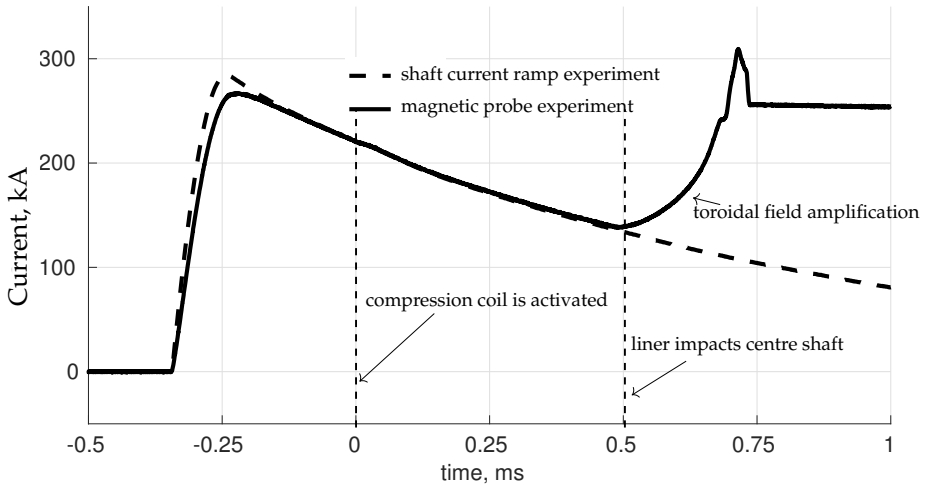


Figure 21. Experimentally measured shaft current as provided by the external circuit (dashed line). Shaft current calculated from toroidal magnetic probe measurement (solid line): $I_{\text{shaft}} = 2\pi r_{\text{probe}} B_\phi / \mu_o$, where $\mu_o = 4\pi \times 10^{-7}\,\text{T}\cdot\text{m}/\text{A}$. Time $t = 0$—compression coil is activated; $t = 0.5$ ms—liner impacts the centre shaft and traps toroidal flux; $t = 0.7$ ms—approximately maximum compression.

Trapping of the toroidal flux in the simulations is demonstrated in Figure 22. The results are shown for the "oblique" landing, nominal set of parameters, nominal geometry of the compression coil assembly (row two in Figure 19), and for toroidal flux introduced instantaneously at $t = 0$. Two contours of the toroidal function F are shown by black lines for several instances during the implosion. The contour values are the same for all plots. The black arrows indicate the direction of the poloidal current. One can see that when the liner and the centre shaft are not in contact, there are separate current loops in the centre shaft and in the liner (Figure 22a). Once the liner impacts the centre shaft and electrical contact is established, current flows through the centre shaft and the liner in a closed loop, and the toroidal magnetic flux enclosed by this loop becomes trapped (parts (b) and (c)). One can also see that a portion of the enclosed flux diffuses into the liner and the centre shaft during the implosion.

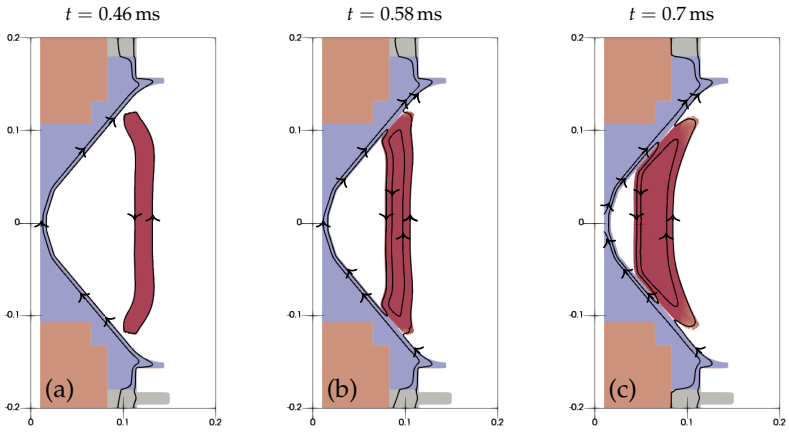


Figure 22. Demonstration of toroidal flux trapping in the simulations. The contours of the toroidal function F are shown by the black lines for two values of F. Arrows indicate the direction of the poloidal current. (**a**) Before liner and centre shaft are in electrical contact—no flux trapping; (**b**) liner and centre shaft are in electrical contact—the toroidal flux enclosed between the structure and the liner is trapped; (**c**) later in the implosion, the liner stays in electrical contact with the centre shaft, and the enclosed flux continues to be trapped.

The effect of the liner's shape on the compression of the toroidal flux is shown in Figure 23. The results are shown for the "oblique" landing and for progressively increasing radii of the deactivated coils (rows 2–5 in Figure 19). In all simulations, the toroidal field was instantly introduced at $t = 0$ and then let to evolve. The figure shows the toroidal function F at the location of the magnetic probe (shown by the red dot in Figure 18b, $r = 21.7$ mm, $z = 20$ mm) which is normalized by its initial value at $t = 0$. It can be seen that the change in the liner shape and, consequently, the change in the shape of the enclosed vacuum cavity does not have a significant effect on the amplification of the toroidal field until very late in the implosion. This can be explained by the fact that the change in the volume of the vacuum cavity, which directly correlates with the change in its inductance, is similar for all cases until very late in the implosion, despite the shape of the liner being different upon impact. After about $t = 0.7$ ms, the results are affected by the change in the shape of the liner.

The comparison between the amplification of the toroidal field obtained in the simulations with that measured in the experiment is shown in Figure 24. Simulation results are shown for both "oblique" and "flat" landings and for nominal and increased radii of the deactivated coils. All simulations are performed with a nominal set of parameters. Toroidal flux is introduced instantaneously at $t = 0$. Both experimental and numerical data are normalized by their values at the time toroidal flux becomes trapped. A small time shift was applied to some numerical curves ($\Delta t_{\max_{\text{shift}}} < 0.02$ ms) to align the flux trapping

time. Overall, the comparison between the simulations and the experiment is good, and the relative error is within a 20% margin as shown in Figure 24b. The experimental data show a maximum toroidal field amplification of 2.25, while for the four simulations presented in Figure 24a, the maximum amplification ranges between 2.4 and 2.6. The amplification of the toroidal field obtained in the simulations is higher than that in the experiment. However, the difference is mainly in the early stage of flux trapping. In later stages, indicated by the light grey shaded region in Figure 24, the rate of increase in the simulations and experiment is similar. The slower initial increase observed in the experiment is likely caused by non-instantaneous attainment of good electrical contact between the liner and the centre shaft.

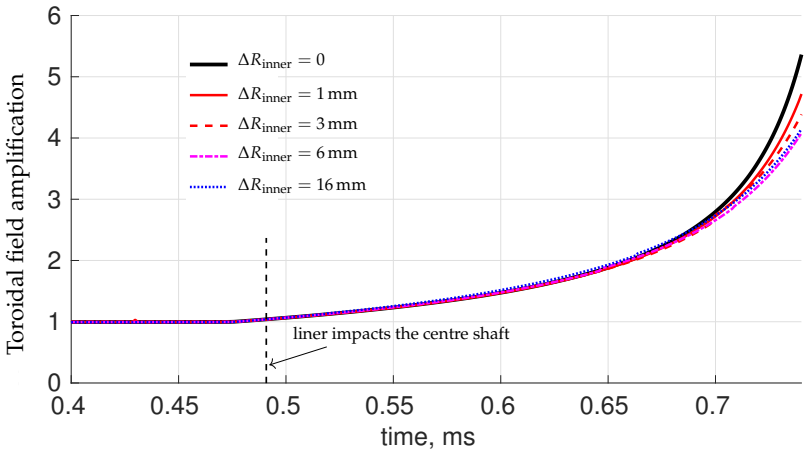


Figure 23. Effect of the liner's shape on the amplification of the toroidal field. Toroidal field function F normalized by its initial value (amplification of the toroidal field) is plotted for $r = 21.7\,\text{mm}$, $z = 20\,\text{mm}$ (marked by the red dot in Figure 18b). The shape of the liner during implosion was modified by increasing the inner radius of the deactivated coils (coils 1, 2, 3, 8, 9, 14, 15, and 16) by ΔR_{inner}. Black solid line—$\Delta R_{\text{inner}} = 0$ (nominal case), red solid line—$\Delta R_{\text{inner}} = 1\,\text{mm}$, red dashed line—$\Delta R_{\text{inner}} = 3\,\text{mm}$, magenta dash-dot line—$\Delta R_{\text{inner}} = 6\,\text{mm}$, blue dotted line—$\Delta R_{\text{inner}} = 16\,\text{mm}$. Time at which the liner comes into contact with the centre shaft is similar for all cases ($0.475\,\text{ms} \leq t_{\text{contact}} \leq 0.480\,\text{ms}$).

3.2.5. Effect of Magnetic Diffusivity of the Liner

The simulation results for the implosion of a lithium ring (see Section 3.1) indicated that the trajectory and shape of the ring are sensitive to the magnetic diffusivity. As such, the effect of magnetic diffusivity is examined in this experiment as well. The results are shown in Figure 25, where parts (a) and (b) correspond to the poloidal and toroidal fields, respectively. The results are shown for the "oblique" landing, nominal set of parameters and nominal geometry of the magnetic coil assembly. Magnetic diffusivity is varied within the range of $0.1 \leq \eta_{\text{cylinder}}\,[\text{m}^2/\text{s}] \leq 0.5$. The plots are shown for $r = 21.7\,\text{mm}$, $z = 20\,\text{mm}$ (marked by the red circle in Figure 18b). One can see that the strength of the poloidal magnetic field increases as the magnetic diffusivity of the liner is increased. This is due to the combined effect of faster diffusion of the magnetic field throughout the liner and a slower implosion. One should note that once the pushing poloidal field diffuses throughout the liner, it starts to act in the opposite direction, i.e., to decelerate the liner. The stronger this field is, the more it affects the shape and trajectory of the liner. Following the evolution of the toroidal field, it can be seen that there is less amplification of the toroidal flux as the liner's magnetic diffusivity is increased. Note that for higher values of magnetic diffusivity, contact between the liner and centre shaft occurs later, so differences between the curves should be interpreted with caution. However, one can see that no toroidal field amplification is observed for $\eta_{\text{cylinder}} = 0.5\,\text{m}^2/\text{s}$.

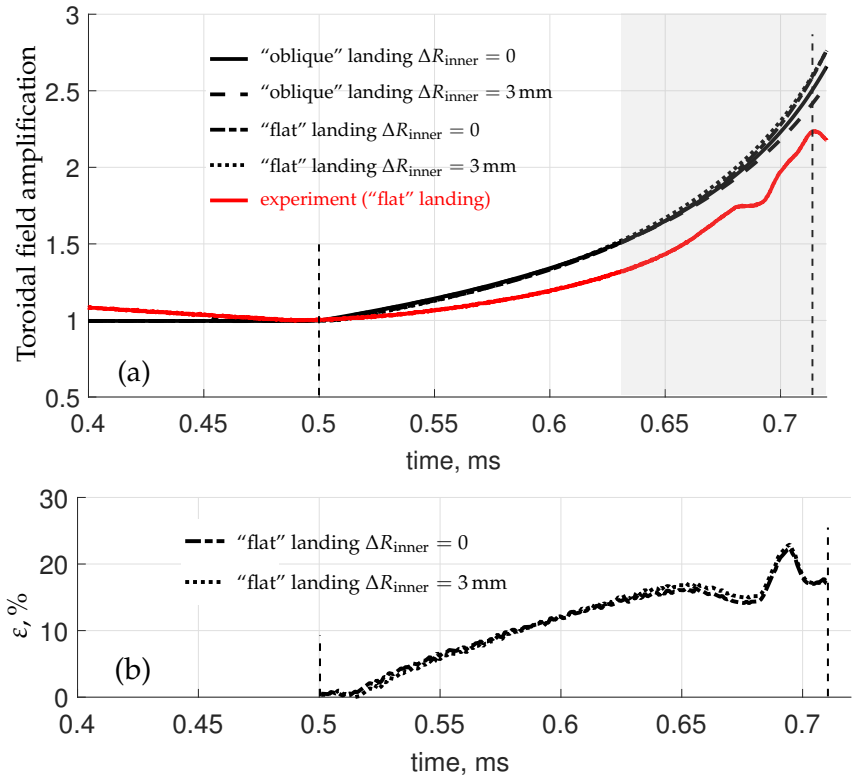


Figure 24. Comparison between the amplification of the toroidal field obtained in the simulation with that obtained in the experiment: (**a**) absolute amplification values A_{sim}, A_{exp}; (**b**) relative error $\varepsilon = (A_{sim} - A_{exp})/A_{exp}$ from the moment toroidal flux is trapped. Simulation results are shown for both "oblique" and "flat" landings and for nominal and increased radii of the deactivated coils. All simulations were performed with the nominal set of parameters. Both experimental and numerical data are normalized by their value at the time when the toroidal flux becomes trapped. Numerical curves are shifted in time ($\Delta t_{max_{shift}} < 0.02$ ms for all curves) to align the time when the flux becomes trapped.

This can be explained by looking at the evolution of the poloidal magnetic field during the implosion in conjunction with the shape and trajectory of the liner. This is shown in Figure 26 for the nominal $\eta_{cylinder} = 0.1\,m^2/s$ (first row) and higher $\eta_{cylinder} = 0.5\,m^2/s$ (second row) magnetic diffusivity of the liner. The magnitude of the poloidal field is shown by a colour-map of the same scale in all plots. Contours of the poloidal flux ψ are also shown for the same values in all plots and are coloured by the magnitude of the poloidal field. When comparing the results obtained at two values of magnetic diffusivity, the following can be observed: (i) a noticeably weaker pushing field for the higher value of magnetic diffusivity, even at early times ($t = 0.05$ s); (ii) the shape of the liner is significantly different by the time it approaches the centre shaft ($t = 0.48$ s); (iii) when the top and bottom of the liner get close to the centre shaft, the soaked through poloidal field is compressed, and this compressed field is stronger for higher magnetic diffusivity of the liner; (iv) for magnetic diffusivity of $\eta_{cylinder} = 0.5\,m^2/s$, the magnetic pressure from the compressed soaked-through magnetic field is sufficient to alter the shape of the liner and to prevent it from impacting the centre shaft; and (v) at later times the liner is noticeably slowed down by the push-back from the soaked poloidal field for the case with higher magnetic diffusivity. As such, for the liner with a magnetic diffusivity of $\eta_{cylinder} = 0.5\,m^2/s$, no electrical contact is established between the liner and the centre shaft (at least for the times being considered), which explains why no compression of the toroidal flux is observed in this case (see Figure 25b).

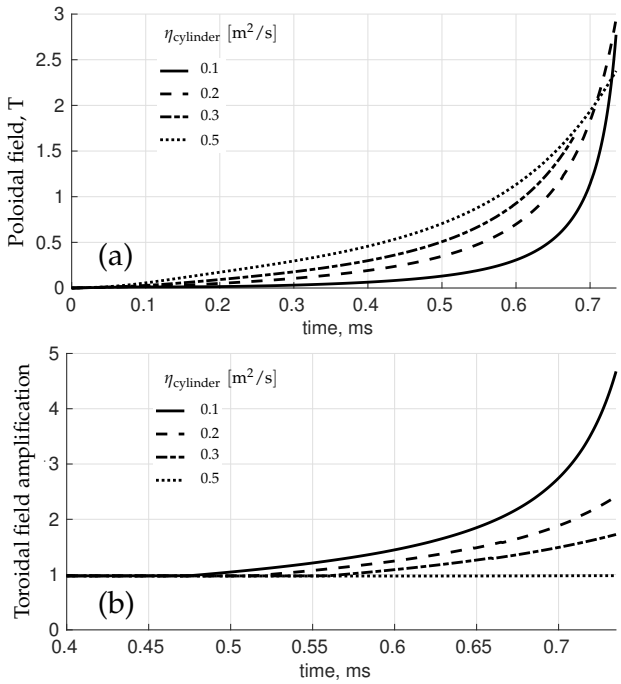


Figure 25. Effect of the liner's magnetic diffusivity. (**a**) Evolution of the poloidal field; (**b**) evolution of the toroidal function F normalized by its initial value (toroidal field amplification). Results are shown for $r = 21.7\,\text{mm}$, $z = 20\,\text{mm}$ (shown by the red dot in Figure 18b). Solid line—$\eta_{\text{cylinder}} = 0.1\,\text{m}^2/\text{s}$, dashed line—$\eta_{\text{cylinder}} = 0.2\,\text{m}^2/\text{s}$, dash-dot line—$\eta_{\text{cylinder}} = 0.3\,\text{m}^2/\text{s}$, dotted line—$\eta_{\text{cylinder}} = 0.5\,\text{m}^2/\text{s}$.

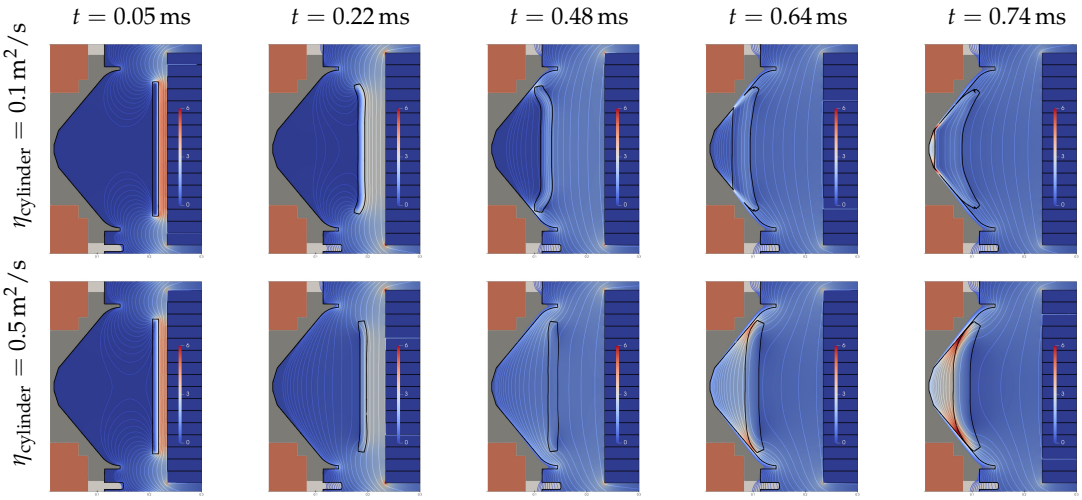


Figure 26. Effect of the liner's magnetic diffusivity on its trajectory and shape during the implosion. First row: nominal magnetic diffusivity $\eta_{\text{cylinder}} = 0.1\,\text{m}^2/\text{s}$; second row: higher magnetic diffusivity of $\eta_{\text{cylinder}} = 0.5\,\text{m}^2/\text{s}$. Magnitude of the magnetic field within the range of $0 \leq |\mathbf{B}| \leq 6\,\text{T}$ is shown by the colour map. Poloidal flux contours coloured by the magnitude of the magnetic field are shown for the same range of values in all plots: $-0.03\,\text{Wb/rad} \leq \psi \leq 0.0001\,\text{Wb/rad}$, 21 contours logarithmically spaced.

4. Summary and Conclusions

In this work, electromagnetic coils driven by an external circuit were implemented into our in-house solver, "mhdCompressibleInterFoam" [20], developed within the OpenFOAM framework. Additional infrastructure was developed to incorporate magnetic diffusion across multiple solid materials. This work was motivated by the construction of LM26 at

General Fusion, which utilizes electromagnetic coils powered by high-voltage capacitor banks to compress magnetized plasma targets.

The solver was applied to simulate two small-scale experiments conducted at General Fusion, which aimed to de-risk components of LM26. The first experiment is the electromagnetic implosion of a lithium ring, aimed at validating the design of the electromagnetic coils and achieving symmetric implosion. The second experiment is the electromagnetic implosion of a hollow lithium cylinder onto an hourglass-shaped central structure (Prototype 0 campaign). In this experiment, the electromagnetic compression coil assembly comprises 16 individual coils connected to high-voltage pulsed power supplies. This enables the manipulation of the shape of the liner during the implosion by deactivating subsets of the coils. A vital part of this experimental campaign was to study the evolution of the toroidal field generated by the poloidal electric current flowing through the centre shaft. The key objective was to demonstrate trapping and compression of the toroidal flux enclosed by the liner and centre shaft once they are in electrical contact. This is a necessary requirement to maintain the stability of a magnetized plasma during compression.

The main conclusions from this work are as follows:

- Two experimental test beds for the electromagnetic implosion of solid lithium rings and hollow cylinders were successfully simulated using the in-house "mhdCompressibleInterFoam" solver developed in OpenFOAM, with the highly deformable solid lithium modelled as a high-viscosity liquid. The simulated trajectories and liner shapes showed good agreement with the experimental results.
- The trapping and compression of the toroidal magnetic flux enclosed between the liner and the centre shaft, achieved in the Prototype 0 experiment, were successfully replicated in simulations. Simulation results provide an upper bound for the compression of toroidal flux by assuming instantaneous electrical contact between the liner and the centre shaft, whereas experimental results indicate that it takes time to establish good electrical contact, which leads to a slower rate of flux compression at early stages. The Prototype 0 experiment demonstrated toroidal field amplification by a factor of 2.25, and simulations reproduced this within a relative error margin of 20%.
- When metal liners are imploded by electromagnetic means, the implosion trajectory is sensitive to the magnetic diffusivity of the liner. Therefore, careful choice of liner magnetic diffusivity is essential for accurate prediction of implosion trajectories.
- When metal liners are imploded by electromagnetic means, a portion of the driving magnetic field soaks through the liner; the amount depends on the implosion speed and the magnetic diffusivity of the liner. As the liner approaches the centre shaft, it compresses the soaked-through magnetic field. This compressed field can be sufficiently strong to alter the shape of the liner, slow its motion, and, under certain conditions, delay or prevent contact between the liner and the centre shaft.

Author Contributions: Conceptualization, V.S., I.V.K., and P.W.F.; methodology, V.S. and I.V.K.; software, V.S.; validation, V.S., D.M.R., and P.W.F.; formal analysis, D.M.R., P.W.F., and V.S.; writing—original draft preparation, V.S.; writing—review and editing, V.S., I.V.K., D.M.R., and P.W.F.; visualization, V.S. and D.M.R. All authors have read and agreed to the published version of the manuscript.

Funding: This work was supported by funding from the Government of Canada through its Strategic Innovation Fund (Agreement No. 811-811346).

Data Availability Statement: Solver and test cases can be provided upon request.

Acknowledgments: The authors would like to acknowledge the entire General Fusion team for making this work possible. In particular, we thank Colin McNally for proofreading the article and for his constructive suggestions which enhanced the clarity of the manuscript.

Conflicts of Interest: All authors were employed by the company General Fusion and declare that the research was conducted in the absence of any commercial or financial relationships that could be construed as a potential conflict of interest.

Abbreviations

The following abbreviations are used in this manuscript:

MTF	Magnetized Target Fusion
MHD	Magnetohydrodynamics

Appendix A. Governing Equations for "mhdCompressibleInterFoam" Solver

The "mhdCompressibleInterFoam" solver is an extension of "compressibleInterFoam", which is a standard solver within the OpenFOAM software. "compressibleInterFoam" is a multi-phase (liquid–gas) hydro solver to model two compressible, immiscible fluids. The interface between the two phases is tracked using a Volume of Fluid (VoF) phase-fraction-based interface-capturing approach [31,43].

Hydro Part ("compressibleInterFoam"):

The mass continuity equation:

$$\frac{\partial \rho}{\partial t} + \nabla \cdot (\rho \mathbf{v}) = 0. \tag{A1}$$

The momentum equation:

$$\frac{\partial (\rho \mathbf{v})}{\partial t} + \nabla \cdot (\rho \mathbf{v}\mathbf{v}) = -\nabla \left(p + \frac{2}{3}\mu \nabla \cdot \mathbf{v} \right) + \nabla \cdot \left[\mu \left(\nabla \mathbf{v} + (\nabla \mathbf{v})^{\mathrm{T}} \right) \right] + \underbrace{\text{Lorentz force}}_{\text{(Equation (A9))}} + \text{gravity} + \text{surface tension}, \tag{A2}$$

where Lorentz force is a source term coming from MHD equations which can be activated separately for each phase. Gravity and surface tension are neglected in this work.

The phase fraction continuity equation:

$$\frac{(\rho \alpha_i)}{\partial t} + \nabla \cdot (\rho \alpha_i \mathbf{v}) = 0, \tag{A3}$$

where subscript i denotes the phase and α is the phase fraction.

The energy equation (optional and can be turned off):

$$\frac{\partial (\rho C_p T)}{\partial t} + \nabla \cdot (\rho \mathbf{v} C_p T) = \nabla \cdot (k \nabla T) + \underbrace{S_T}_{\text{source terms}} + \underbrace{P_{ohm}}_{\text{Ohmic heating (Equation (A10))}}, \tag{A4}$$

where Ohmic heating is a source term coming from MHD equations which can be activated separately for each phase. The equation of state:

$$\rho_i = \rho_i(p, T), \tag{A5}$$

where for each phase "i" there are several available equations of state. In this work, the ideal gas equation of state is used for the gas (vacuum) phase and the barotropic Tait equation [33] is used for the liquid (lithium) phase.

In Equations (A1)–(A5), ρ, μ, C_p, and k are density, viscosity, heat capacity, and thermal conductivity, respectively. Both fluids (gas and liquid) are treated as a single fluid "mixture" with properties varying in space according to the volume fraction of each phase as given in Equation (A6). With this approach, the interface is not treated as a boundary, and no

boundary conditions are prescribed at it; instead, it is treated as a discontinuity in fluid properties [43].

$$\rho = \alpha_1\rho_1 + \alpha_2\rho_2, \;\; \mu = \alpha_1\mu_1 + \alpha_2\mu_2, \;\; k = \alpha_1 k_1 + \alpha_2 k_2, \tag{A6}$$

where subscripts 1 and 2 denote the two fluids (e.g., liquid and gas) and $\alpha_1 + \alpha_2 = 1$.

MHD Part (extension to the "compressibleInterFoam"):

Evolution of the toroidal function F (Equation (A7)) and the poloidal flux per radian ψ (Equation (A8)):

$$\frac{1}{r^2}\frac{\partial F}{\partial t} + \left[\nabla\cdot\left(\frac{\mathbf{v}}{r^2}F\right) - \nabla\cdot\left(\frac{\eta}{r^2}\nabla F\right)\right] - \nabla\cdot\left(\omega\mathbf{B}_{\text{pol}}\right) = 0, \tag{A7}$$

$$\frac{\partial\psi}{\partial t} + \mathbf{v}\cdot\nabla\psi - \eta\left[r^2\nabla\cdot\left(\frac{1}{r^2}\nabla\psi\right)\right] = 0, \tag{A8}$$

where $\eta[\mathrm{m}^2/\mathrm{s}]$ is the magnetic diffusivity, $\mathbf{v}$ is the velocity, $\omega = v_\phi/r$ is the angular velocity, $\mathbf{B}_{\text{pol}} = \nabla\psi\times\nabla\phi$ is the poloidal component of magnetic field, and the cylindrical coordinate system (r,ϕ,z) is used.

$$\begin{gathered}\text{Lorentz force}\left[\frac{\mathrm{N}}{\mathrm{m}^3}\right] = -\frac{\nabla(F^2)}{2\mu_o r^2} - \frac{1}{\mu_o r^2}\Delta^*\psi\nabla\psi + \frac{1}{\mu_o}\left(\mathbf{B}_{\text{pol}}\cdot\nabla F\right)\nabla\phi, \\ \text{where } \Delta^*\psi = r^2\nabla\cdot\left(\frac{1}{r^2}\nabla\psi\right).\end{gathered} \tag{A9}$$

$$\text{Ohmic power}\left[\frac{\mathrm{kg}}{\mathrm{s}^3\mathrm{m}}\right] = P_{ohm} = \frac{\eta}{\mu_o}\left(\frac{|\nabla F|^2}{r^2} + \frac{(\Delta^*\psi)^2}{r^2}\right). \tag{A10}$$

Similar to other properties, the magnetic diffusivity η varies in space according to the volume fraction of each phase as:

$$\eta = \alpha_1\eta_1 + \alpha_2\eta_2, \tag{A11}$$

where subscripts 1 and 2 denote the two fluids (gas (vacuum) and liquid (lithium liner)) and $\alpha_1 + \alpha_2 = 1$. To extend this approach to also model magnetic diffusion into the rigid multi-material structure, the mesh is fitted to the geometry of the structure, so each grid cell is either strictly inside or outside the structure. Different materials are represented by the corresponding dedicated cell set, and the magnetic diffusivity of a specific material is assigned to each set at every time step. The momentum equation is not solved for the cells representing the rigid structure, enforcing zero velocity. As such, in the grid cells representing the rigid structure, only the equations for magnetic field evolution (Equations (A7) and (A8)) are solved.

Appendix B. Analytical Solution for RLC Circuit

The governing equation and the corresponding analytical solution for the electric current in a theoretical RLC circuit are detailed below. For the case of a series RLC circuit, the electric current is governed by the following second order differential equation (Equation (A12)):

$$\frac{d^2}{dt^2}I(t) + \frac{R_{\text{eff}}}{L_{\text{eff}}}\frac{d}{dt}I(t) + \frac{1}{L_{\text{eff}}C_{\text{eff}}}I(t) = 0, \text{ where} \tag{A12}$$

R_{eff}, L_{eff}, and C_{eff} are the effective resistance, inductance, and capacitance of the equivalent circuit. Equation (A12) can be rewritten as Equation (A13):

$$\frac{d^2}{dt^2}I(t) + 2\beta\frac{d}{dt}I(t) + \omega_0^2 I(t) = 0, \text{ where } \beta = \frac{R_{\text{eff}}}{2L_{\text{eff}}},\ \omega_0 = \frac{1}{\sqrt{L_{\text{eff}}C_{\text{eff}}}}. \tag{A13}$$

The nature of the solution depends on the parameter $\zeta \equiv \beta/\omega_0$, where for $\zeta < 1$ (under-damped response), the general solution for Equation (A13) is given by Equation (A14):

$$I(t) = A_1 e^{-\beta t}\cos(\omega_d t) + A_2 e^{-\beta t}\sin(\omega_d t),\ \omega_d = \sqrt{\omega_0^2 - \beta^2},\ \text{where} \tag{A14}$$

A_1 and A_2 are constants defined by the initial conditions. In the test case, the initial conditions are zero current and the capacitor charged to voltage V_o (Equation (A15)):

$$I(t=0) = 0 \text{ and } Q(t=0) = V_o\, C_{\text{eff}}. \tag{A15}$$

With initial conditions given by Equation (A15), the solution of Equation (A14) is (Equation (A16)):

$$I(t) = -\frac{\beta^2 + \omega_d^2}{\omega_d} V_o\, C_{\text{eff}}\, e^{-\beta t}\ \sin(\omega_d\, t). \tag{A16}$$

For a circuit that includes a diode, when the diode is on, the RLC circuit switches to an RL circuit, as shown by the blue loop in Figure 4b. Electric current then decays according to the corresponding effective resistance and inductance as per (Equation (A17)):

$$I(t > t_d) = I_d e^{-R_{\text{eff}}(t-t_d)/L_{\text{eff}}}, \tag{A17}$$

where t_d is the time when the diode is activated, I_d is the value of the electric current when the diode is activated, and R_{eff} and L_{eff} are the effective resistance and inductance of the corresponding RL circuit (Figure 4b).

Appendix C. Supplementary Plots

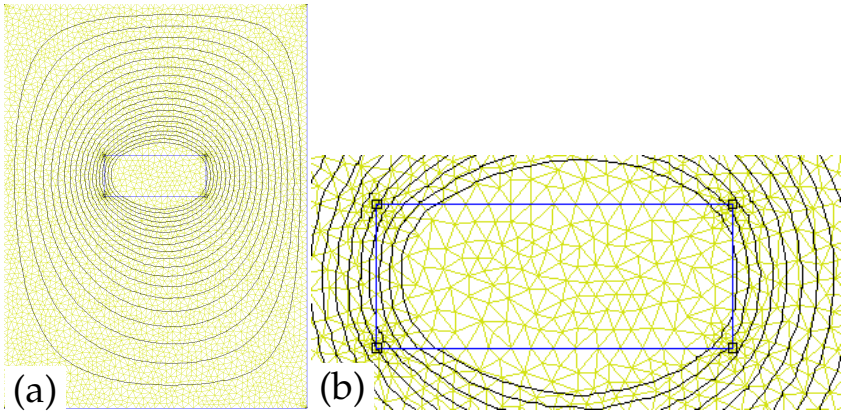


Figure A1. Computational mesh used in FEMM simulations for the coil implementation verification case. (**a**) Entire domain; (**b**) zoomed in view of the coil region.

References

1. Miller, R.L.; Krakowski, R.A. Assessment of the Slowly-Imploding Liner (LINUS) Fusion Reactor Concept. In Proceedings of the 4th ANS Topical Meeting on the Technology of Nuclear Fusion, King of Prussia, PA, USA, 14–17 October, 1980 .
2. Turchi, P.J.; Cooper, A.L.; Ford, R.D.; Jenkins, D.J.; Burton, R.L. Review of the Liner Implosion Program. In *MegaGauss Physics and Technology*; Plenum Press: New York, NY, USA; London, UK, 1980.

3. Kirkpatrick, R.C.; Lindemuth, I.R.; Ward, M.S. Magnetized Target Fusion: An Overview. *Fusion Technol.* **1997**, *27*, 201–214. [CrossRef]
4. Siemon, R.E.; Lindemuth, I.R.; Schoenberg, K.F. Why Magnetized Target Fusion Offers a Low-Cost Development Path for Fusion Energy. *Comments Plasma Phys. Control. Fusion* **1999**, *18*, 363–386.
5. Wurden, G.A.; Hsu, S.C.; Intrator, T.P.; Grabowski, T.C.; Degnan, J.H.; Domonkos, M.; Turchi, P.J.; Campbell, E.M.; Sinars, D.B.; Herrmann, M.C.; et al. Magneto-Inertial Fusion. *J. Fusion Energy* **2016**, *35*, 69–77. [CrossRef]
6. Statham, G.; White, S.; Adams, R.B.; Thio, Y.C.F.; Alexander, R.; Fincher, S.; Philips, A.; Polsgrove, T. Engineering of the Magnetized Target Fusion Propulsion System. In Proceedings of the 39th AIAA/ASME/SAE/ASEE Joint Propulsion Conference and Exhibit, Huntsville, AL, USA, 20–23 July 2023.
7. Intrator, T.; Zhang, S.Y.; Furno, I.; Hsu, S.C.; Sanchez, P.G.; Taccetti, J.M.; Tuszewski, M.; Waganaar, W.J.; Wurden, G.A.; Degnan, J.H.; et al. A High Density Field Reversed Configuration (FRC) Target for Magnetized Target Fusion: First Internal Profile Measurements of a High Density FRC. *Phys. Plasmas* **2004** *11*, 2580–2585. [CrossRef]
8. Degnan, J.H.; Amdahl, D.J.; Domonkos, M.; Grabowski, C.; Ruden, E.L.; White, W.M.; Wurden, G.A.; Intrator, T.P.; Sears, J.A.; Weber, T.; et al. Recent Magneto-Inertial Fusion Experiments on FRCHX. In Proceedings of the 24th IAEA Fusion Energy Conference, San Diego, CA, USA, 8–13 October 2012.
9. Grabowski, C.; Degnan, J.H.; Domonkos, M.; Amdahl, D.; Ruden, E.L.; Wurden, G.A.; Weber, T.E. The Field-reversed Configuration Heating Experiment on Shiva Star In Proceedings of IEEE International Conference on Plasma Science, Banff, AB, Canada, 19–23 June 2016.
10. Howard, S.J.; Reynolds, M.; Froese, A.; Zindler, R.; Hildebrand, M.; Mossman, A.; Donaldson, M.; Tyler, T.; Froese, D.; Eyrich, C.; et al. Measurement of Spherical Tokamak Plasma Compression in the PCS-16 Magnetized Target Fusion Experiment. *Nucl. Fusion* **2024**, *65*, 016029. [CrossRef]
11. Mangione, N.S.; Wu, H.; Preston, C.; Lee, A.M.D.; Entezami, S; Ségas, R.; Forysinski, P.W.; Suponitsky, V. Shape Manipulation of a Rotating Liquid Liner Imploded by Arrays of Pneumatic Pistons: Experimental and Numerical Study. *Fusion Eng. Des.* **2023**. [CrossRef]
12. Laberge, M. Magnetized Target Fusion with a Spherical Tokamak. *J. Fusion Energy* **2018** *38*, 199–203. [CrossRef]
13. Turchi, P.J. Progress and Issues with Pulsed Magnetic Fusion. *Phys. Plasmas* **2025** *32*, 022507. [CrossRef]
14. Wurzel, S.E.; Hsu, S.C. Continuing Progress Toward Fusion Energy Breakeven and Gain as Measured Against the Lawson Criteria. *arXiv* **2025**, arXiv:2505.03834v3. [CrossRef]
15. Froese, A.; Reynolds, M.; Suponitsky, V.; Dick, J.-S.; Segas, R.; Khalzov, I.V.; Sirmas, N.; Ross, D.; Roberts, D.; Brennan, D. Expected MHD Stability and Error Field Penetration in LM26 Magnetized Target Fusion Experiment at General Fusion, In Proceedings of the 66th Annual Meeting of the APS Division of Plasma Physics, Atlanta, GA, USA, 7–11 October 2024. Available online: https://meetings.aps.org/Meeting/DPP24/Session/PP12.68 (accessed on 18 August 2025).
16. OpenFOAM. The OpenFOAM Foundation. Available online: https://cfd.direct (accessed on 18 August 2025).
17. Suponitsky, V.; Barsky, S.; Froese, A. Richtmyer–Meshkov Instability of a Liquid-gas Interface Driven by a Cylindrical Imploding Pressure Wave. *Comp Fluids* **2014**, *89*, 1–19. [CrossRef]
18. Suponitsky, V.; Avital, E.J.; Plant, D.; Munjiza, A. Pressure Wave in Liquid Generated by Pneumatic Pistons and Its Interaction with a Free Surface. *Int. J. Appl. Mech.* **2017**, *9*, 1750037. [CrossRef]
19. Avital, E.J.; Suponitsky, V.; Khalzov, I.V.; Zimmermann, J.; Plant, D. On the Hydrodynamic Stability of an Imploding Rotating Circular Cylindrical Liquid Liner. *Fluid Dyn. Res.* **2020**, *52*, 055505. [CrossRef]
20. Suponitsky, V.; Khalzov, I.V.; Avital, E.J. Magnetohydrodynamics Solver for a Two-Phase Free Surface Flow Developed in OpenFOAM. *Fluids* **2022**, *7*, 210. [CrossRef]
21. Ryakhovskiy, A.I.; Schmidt, A.A. MHD Supersonic Flow Control: OpenFOAM simulation. *Trudy ISP RAS* **2016**, *28*, 197–206. [CrossRef]
22. Garrido González, D.; Suárez Cambra, D.; Futatani, S. Non-linear MHD Simulations of Magnetically Confined Plasma using OpenFOAM. In Proceedings of the 7th BSC Severo Ochoa Doctoral Symposium, Barcelona, Spain, 5 May 2020; pp. 61–62. Available online: https://upcommons.upc.edu/handle/2117/331029 (accessed on 18 August 2025).
23. Blishchik, A.; van der Lans, M.; Kenjeres, S. An Extensive Numerical Benchmark of the Various Magnetohydrodynamic Flows. *Int. J. Heat Fluid Flow* **2021**, *90*, 108800. [CrossRef]
24. Suárez Cambra, D; Khodak, A.; Mas de les Valls, E.; Batet, L. A Formal Verification and Validation of a Low Magnetic Reynolds Number MHD Code for Fusion Applications. *IEEE Trans. Plasma Sci.* **2022**, *50*, 4206–4212. [CrossRef]
25. Aslani, K.E.; Sarris, I.E.; Tzirtzilakis, E. On the Development of OpenFOAM Solvers for Simulating MHD Micropolar Fluid Flows with or without the Effect of Micromagnetorotation. *arXiv* **2025**, arXiv:2504.14543. [CrossRef]
26. Wynne, B.; Saenz, F.; Al-Salami, J.; Xu, Y.; Sun, Z.; Hu, C.; Hanada, K.; Kolemen, E. FreeMHD: Validation and Verification of the Open-source, Multi-domain, Multi-phase Solver for Electrically Conductive Flows. *Phys. Plasmas* **2025**, *32*, 013907. [CrossRef]

27. Boronski, P.; Tuckerman, L.S. Magnetohydrodynamics in a Finite Cylinder: Poloidal-Toroidal Decomposition. In Proceedings of the European Conference on Computational Fluid Dynamics ECCOMAS CFD 2006, Egmond aan Zee, The Netherlands, 5–8 September 2006 .
28. Boronski, P. A Method Based on Poloidal-toroidal Potentials Applied to the von Kármán flow in a Finite Cylinder Geometry. Ph.D. Thesis, Ecole Polytechnique, Orsay, France, 2005 . Available online: https://pastel.archives-ouvertes.fr/tel-00162594/document (accessed on 18 August 2025).
29. Dunlea, C.; Khalzov, I.V. A Globally Conservative Finite Element MHD Code and Its Application to the Study of Compact Torus Formation, Levitation and Magnetic Compression. *arXiv* **2019**, arXiv:1907.13283.
30. Meeker, D.C. Finite Element Method Magnetics, User's Manual, Version 4.2. 2018. Available online: http://www.femm.info/wiki/HomePage (accessed on 18 August 2025).
31. Greenshields, C.J.; Weller, H.G. Notes on Computational Fluid Dynamics: General Principles, CFD Direct. 2022. Available online: https://doc.cfd.direct/notes/cfd-general-principles/ (accessed on 18 August 2025).
32. Dick, J-S; Sirmas, N.; Bernard, S.; Santos, L.; Forysinski, P. Electromagnetic Lithium Ring Compression for Magnetized Target Fusion Application: Trajectories. In Proceedings of the ASME Pressure Vessels & Piping Conference, Bellevue, Washington, DC, USA, 29 July–2 August 2024.
33. Tait, P.G. *Report on Some of the Physical Properties of Fresh Water and of Sea Water*; Report on the Scientific Results of the Voyage of the H.M.S. Challenger during the Years 1873-76: Physics and Chemistry, 1; Johnson Reprint Corporation: New York, NY, USA, 1965. Available online: https://books.google.ca/books?id=zMgUAQAAIAAJ (accessed on 18 August 2025).
34. Itoh, Y.; Kanagawa, T.; Miyazaki, K.; Fujii-E, Y. Cavitation in Cylindrical Liquid Metal Shell Imploded for Axial Magnetic Flux Compression. *J. Nucl. Sci. Technol.* **1982**, *19*, 1–10. [CrossRef]
35. Chi, T.C.; Electrical Resistivity of Alkali Elements. *J. Phys. Chem. Ref. Data* **1979**, *8*, 339–438. [CrossRef]
36. Schaeffer, A.J.; Talmadge, W.B,; Temple, S.R.; Deemyad, S. High Pressure Melting of Lithium. *Phys. Rev. Lett.* **2012**, *109*, 185702. [CrossRef] [PubMed]
37. Jerabek, P.; Burrows, A.; Schwerdtfeger, P. Solving a Problem with a Single Parameter: A Smooth *bcc* To *fcc* Phase Transition for Metallic Lithium. *Chem. Commun.* **2022**, *58*, 13369–13372. [CrossRef] [PubMed]
38. Johnson, G.R.; Cook, W.H. A Constitutive Model and Data for Metals Subjected to Large Strains, High Strain Rates and High Temperatures. In Proceedings of the 7th International Symposium on Ballistics, The Hague, The Netherlands, 19–21 April 1983; pp. 541–547.
39. Miao, Y.; Sexsmith, M.; Hartono, S.; Preston, C.; Tsai, B.; Sirmas, N. Strain-rate-dependant Parameters of Lithium as a Plasma Facing Material for Magnetized Target Fusion Application. In Proceedings of the ASME Pressure Vessels & Piping Conference, Bellevue, Washington, DC, USA, 29 July–2 August 2024.
40. Brennan, D.; Froese, A.; Reynolds, M.; Barsky, S.; Wang, Z.; Delage, M.; Laberge, M. Stable Compression of a Spherical Tokamak Plasma. *Nucl. Fusion* **2020** *60*, 046027. [CrossRef]
41. Brennan, D.; Froese, A.; Reynolds, M.; Barsky, S.; Wen, A.; Delage, M.; Laberge, M. A stable Corridor for Toroidal Plasma Compression. *Nucl. Fusion* **2021** *61*, 046027. [CrossRef]
42. Dick, J-S.; Sirmas, N.; Bernard, S.; Miao, Y.; Santos, L.; Hobbis, J.; Preston, C.; Lee, A.; Cameron, S.; Forysinski, P. Simulation of Electromagnetic Lithium Cylinder Compression for Applications in Magnetized Target Fusion. In Proceedings of the ASME Pressure Vessels & Piping Conference, Montreal, QC, Canada, 20–25 July 2025.
43. Ferziger, J.H.; Perić, M. *Computational Methods for Fluid Dynamics*; Springer: Berlin/Heidelberg, Germany; New York, NY, USA, 1997; ISBN 3-540-59434-5.

Disclaimer/Publisher's Note: The statements, opinions and data contained in all publications are solely those of the individual author(s) and contributor(s) and not of MDPI and/or the editor(s). MDPI and/or the editor(s) disclaim responsibility for any injury to people or property resulting from any ideas, methods, instructions or products referred to in the content.